PONTIFICIA UNIVERSIDAD CATOLICA DE CHILE
ESCUELA DE INGENIERIA

NONLINEAR MODELING OF REINFORCED CONCRETE SHEAR WALLS USING AN IMPROVED FIBER ELEMENT

JORGE ANDRÉS VÁSQUEZ GONZÁLEZ

Thesis submitted to the Office of Research and Graduate Studies in partial fulfillment of the requirements for the Degree of Master of Science in Engineering

Advisor:
JUAN CARLOS DE LA LLERA MARTÍN

Santiago de Chile, (January,2015)

PONTIFICIA UNIVERSIDAD CATOLICA DE CHILE
ESCUELA DE INGENIERIA

NONLINEAR MODELING OF REINFORCED CONCRETE SHEAR WALLS USING AN IMPROVED FIBER ELEMENT

JORGE ANDRÉS VÁSQUEZ GONZÁLEZ

Members of the Committee:

JUAN CARLOS DE LA LLERA MARTÍN

MATÍAS ANDRÉS HUBE GINESTAR

LEONARDO MAXIMILIANO MASSONE SANCHEZ

IGNACIO HECTOR LIRA CANGUILHEM

Thesis submitted to the Office of Research and Graduate Studies in partial fulfillment of the requirements for the Degree of Master of Science in Engineering

Santiago de Chile, (January, 2015)

I dedicate this to my family for their endless support.

ACKNOWLEDGEMENTS

I'm thankful to my advisor who always encouraged me to solve complex problems which was absolutely necessary in this process. I would also like to show gratitude to all the professors at Pontificia Universidad Católica de Chile who showed me their enthusiasm and answered all my questions throughout my undergraduate studies.

I'm grateful to all my friends and colleagues which I have very pleasant and interesting talks with.

Most important of all, none of this could have happened without my family; my parents who made me the person I'm now and my sister and brother who always supported me in every step of my life.

Finally, this research has been sponsored by the National Research Center for Integrated Natural Disaster Management CONICYT/FONDAP/15110017 and by Fondecyt grant #1110377

TABLE OF CONTENTS

LIST OF TABLES

LIST OF FIGURES

RESUMEN

Los muros de corte de hormigón armado (RC) son de uso común, ya que proporcionan una alta rigidez lateral y han demostrado resistir cargas sísmicas severas. En los últimos años, con el creciente número de edificios altos, estos muros se han vuelto más delgados que nunca. Sin embargo, los típicos modelos no lineales para muros son complejos y computacionalmente exigentes, por lo que un modelado preciso y eficiente de estos elementos es absolutamente necesario para evaluar y predecir de forma rápida el comportamiento de los edificios a base de muros. Aprovechando el aumento de la esbeltez, se programó el modelo clásico de fibra y se analizó en detalle la producción de objetividad en los resultados dadas las condiciones de carga comunes resistidas por muros, por ejemplo, alta carga axial y diagrama trapezoidal de momento entre pisos en el caso de un típico edificio residencial chileno, o cargas axiales muy bajas en muros ensayados en laboratorios. Además, para evaluar el corte, se añadió un modelo basado en la teoría de campo de compresiones modificada. Este documento muestra la formulación del modelo propuesto y su validación experimental con diferentes ensayos cíclicos descritos en la literatura. Después de extensivos análisis, se encontró que con el fin de obtener respuestas objetivas, las técnicas de regularización basadas en energía tuvieron que ser modificadas, y los efectos no lineales como el pandeo y fractura de barras de acero, el aplastamiento del hormigón y los efectos de penetración de deformaciones fueron obligatorios para replicar las curvas cíclicas experimentales. Por lo tanto, el modelo es muy atractivo para generar curvas de fragilidad de estos edificios.

ABSTRACT

Reinforced concrete (RC) shear walls are of common use because they provide high lateral stiffness and have proven to withstand severe seismic loads. In recent years, with the growing number of taller buildings, these walls have become more slender than ever. However, common nonlinear models for shear walls are very complex and computationally demanding, so, an accurate and efficient modeling of these elements is absolute necessary to quickly assess and predict the performance of buildings based on RC walls. Taking advantage of the increase in slenderness, the classic fiber model was programmed and it was analyzed in detail the production of objective results under the common loading conditions underwent by walls e.g. high axial loads and trapezoidal moment diagram between stories in case of a typical Chilean residential building, or very low axial loads in some experimentally tested walls. Moreover, to account for shear deformations, model based on the modified compression field theory was used. This document shows the formulation of the proposed model and its experimental validation with different cyclic tests reported in the literature. It was found that in order to get objective responses in the cases just mentioned, the regularization techniques based on fracture energy had to be modified, and all kinds of nonlinearities like buckling and fracture of steel bars, concrete crushing and strain penetration effects were mandatory to replicate experimental cyclic curves. Therefore the model is very attractive for generating fragility curves of these buildings.

1. INTRODUCTION

Reinforced concrete (RC) residential shear wall buildings are commonly used in seismic countries where the cost of materials and human labor still makes them very competitive relative to other types of structures. These structures also became well known in the seismic arena after their good behavior in previous earthquakes, such as the 1985, Chile earthquake (Wood, Wight, & Moehle, 1987). Inherited from this success, most residential buildings in Chile are still based on RC shear walls deployed in plan as a fish-bone like structure, i.e., with a couple of longitudinal central corridor walls, and a number of transverse RC walls separating apartments, and sometimes dividing interior spaces. Although most of these buildings behaved well again during the 2010 Chile earthquake, about 2% of the close to three thousand building taller than five stories built after year 2010 suffered severe structural damage (Jünemann, Hube, Llera, & Kausel, 2010), with one complete collapse (Song, Pujol, & Lepage, 2012).

The observed damage in these RC shear wall buildings was certainly unexpected. Some walls behaved in a brittle manner, with buckling and rupture of the longitudinal reinforcement at the wall boundaries and web, leading in some cases to settlement and leaning of the structures due to the vertical misalignment between the upper and lower portions of the damaged walls (Sherstobitoff, Cajiao, & Adebar, 2012). Indeed, no structural model used by the profession in design did anticipate this behavior, though such behavior was reported earlier in the literature (Bertero, 1980). When subjected to high axial stresses, shear walls do behave in a brittle manner (Alarcon, Hube, & de la Llera, 2014; Su & Wong, 2007; Zhang & Wang, 2000) and the role of boundary confinement may not be sufficient to recover a ductile behavior (Arteta, To, & Moehle, 2014).

Although structural models used currently in design did not anticipate this behavior, the use of models and software to account for the nonlinear dynamic building behavior are

becoming more common today in the profession. It is still a matter of research if such models are capable, or not, of identifying critical zones in these structures and their possible brittle failure modes. Modeling of detailed inelastic behavior of RC elements and their 3D interaction within a structure is still a difficult task, for reasons such as: 1) complex 3D constitutive relationships are not sufficiently validated; 2) all constitutive material relationships are nonlinear: concrete changes by cracking and softening, steel bars yield, buckle and then fracture, loss of bonding and slippage occurs, and numerical convergence under these effects is difficult to guarantee; 3) the response depends on the history of loads and the transient problem still requires substantial computational effort; and 4) the validation of the results of an inelastic dynamic response is still cumbersome and difficult. Therefore, the complete 3D nonlinear dynamic response of a shear wall building with hundreds of thousands of degrees of freedom stills seems unsuitable for the common practice; even for research in some cases. However, since damage in these buildings during 2010 tended to be localized, the inelastic building response was controlled by a few inelastic zones within the structure, usually at walls in the lower levels.

Several models to study the response of RC elements and structures have been proposed and implemented in available software (Diana, 2011; Soltani, Behnamfar, Behfarnia, & Berahman, 2011). These models need to satisfy the following conditions: 1) responses have to be objective, i.e., be independent on the mesh size or number of integration points; 2) the need for calibration has to be minimum, so that the model can be used to predict the behavior of non-tested structures; and 3) the computational demand has to be as low as possible while keeping accuracy.

Because of its simplicity (e.g., one dimensional constitutive relationships), robustness, and low memory usage (typically one element per story is enough), a force based fiber element (FFE) is preferred in several situations. Many analysts have used the FFE to model shear walls (Belmouden & Lestuzzi, 2007; Brueggen, 2009; Jiang & Kurama, 2010; Mazars, Kotronis, Ragueneau, & Casaux, 2006; R. S. Mullapudi, Ayoub, &

Belarbi, 2008), with special consideration of shear deformations, which is the major problem arising from the use of a FFE.

Another relevant issue arising from fiber and other elements models, when softening of materials is present, is the localization observed in the pure axial case ((Jansen & Shah, 1997), (Nakamura & Higai, 2001)), and in bending (Coleman & Spacone, 2001). Localization implies unloading of the neighboring elastic components as the inelastic section of an element softens.

In order to develop a simple, efficient, and accurate model with few calibration requirements for analyzing reinforced concrete shear walls, a new force-based wall element (FWE) comprising the FFE and a shear model was developed in MATLAB. This thesis presents the analytical formulation of the FWE along with the inelastic force-deformation constitutive laws of the materials used. In the analysis, the problem of objective responses and some algorithms for coupling shear, axial and flexure components are considered, and an experimental validation of the FWE is presented.

Moreover, different analyses of shear walls described earlier in the literature are used to validate the results of this model, while the different computer routines, for pure fiber analyses were validated using OpenSees (McKenna, Fenves, & Scott, 2000).

2. FORMULATION OF THE FWE

The FWE presented herein is based on the flexibility based structural element developed elsewhere (Spacone, Filippou, & Taucer, 1996), and adopted using a section nonlinear model aimed to evaluate the shear component, while torsion in the element is assumed elastic. Figure 2-1 shows constraints used to transform a 12 g.d.l. element into a statically supported 6 g.d.l element and for simplicity in notation, the element with 6 g.d.l. will be used as the FWE in this thesis. Please note that the mathematical relation between the two elements is straightforward, i.e., $\boldsymbol{Q}_{12} = \boldsymbol{T}_{12x6}\boldsymbol{Q}_6$, where $\boldsymbol{Q}_{12}, \boldsymbol{Q}_6$ (shown in Figure 2-1) are the nodal forces of the 12 and 6 g.d.l element respectively and $\boldsymbol{T}_{12x6}$ is a linear transformation matrix. As stated before, the element forces for the

FWE, $\boldsymbol{Q}_6$, will be treated simply by $\boldsymbol{Q}$. For a statically supported element, and in particular for the FWE, the flexibility method requires the application of 3 main equations in the following order; 1) the equilibrium equation (Equation 1):

$$\boldsymbol{D}(x) = \begin{bmatrix} N(x) \\ M_y(x) \\ M_z(x) \\ V_y(x) \\ V_z(x) \\ T(x) \end{bmatrix} = \begin{bmatrix} 1 & 0 & 0 & 0 & 0 & 0 \\ 0 & 1 & 0 & 0 & x-L & 0 \\ 0 & 0 & 1 & L-x & 0 & 0 \\ 0 & 0 & 0 & 1 & 0 & 0 \\ 0 & 0 & 0 & 0 & 1 & 0 \\ 0 & 0 & 0 & 0 & 0 & 1 \end{bmatrix} \begin{bmatrix} N^e \\ M_y^e \\ M_z^e \\ V_y^e \\ V_z^e \\ T^e \end{bmatrix} = \boldsymbol{b}(x)\boldsymbol{Q} \qquad (1)$$

where $\boldsymbol{D}(x)$ is the section force vector, x is the distance from the bottom along the element length, L, $\boldsymbol{b}(x)$ is the equilibrium matrix, $\boldsymbol{Q}$ is the element force vector, N^e, V_y^e, V_z^e represent axial and shear forces respectively, M_y^e, M_z^e, bending moments and T^e, torsional moment—the same order than section forces $\boldsymbol{D}(x)$. 2) The force-deformation relation (Equation 2):

$$\boldsymbol{d}(x) = \begin{bmatrix} \varepsilon(x) \\ \kappa_y(x) \\ \kappa_z(x) \\ \gamma_z(x) \\ \gamma_y(x) \\ \gamma_x(x) \end{bmatrix} = \begin{bmatrix} \left[\boldsymbol{f}_{AF}(x)\right]_{3x3} & \mathbf{0} & \mathbf{0} & \mathbf{0} \\ \mathbf{0} & f_{S_y}(x) & 0 & 0 \\ \mathbf{0} & 0 & f_{S_z}(x) & 0 \\ \mathbf{0} & 0 & 0 & f_T(x) \end{bmatrix} \cdot \boldsymbol{D}(x) \qquad (2)$$

where $\boldsymbol{d}(x)$ is the section deformation vector, $\varepsilon, \kappa,$ and γ represent the axial, curvature, and shear deformations of the section, $\boldsymbol{f}_{AF}$ is the section flexibility matrix due to the bending-compression component; and f_{S_y}, f_{S_z}, and f_T are the section shear flexibilities in the y- and z- directions, respectively, and the torsional flexibility. 3) the compatibility equation, $\boldsymbol{q} = \boldsymbol{F}\boldsymbol{Q}$, where $\boldsymbol{q}$ is the element displacement vector, and $\boldsymbol{F} = \int_0^L \boldsymbol{b}(x)^T \boldsymbol{f}(x) \boldsymbol{b}\,(x)dx$ is the element flexibility matrix.

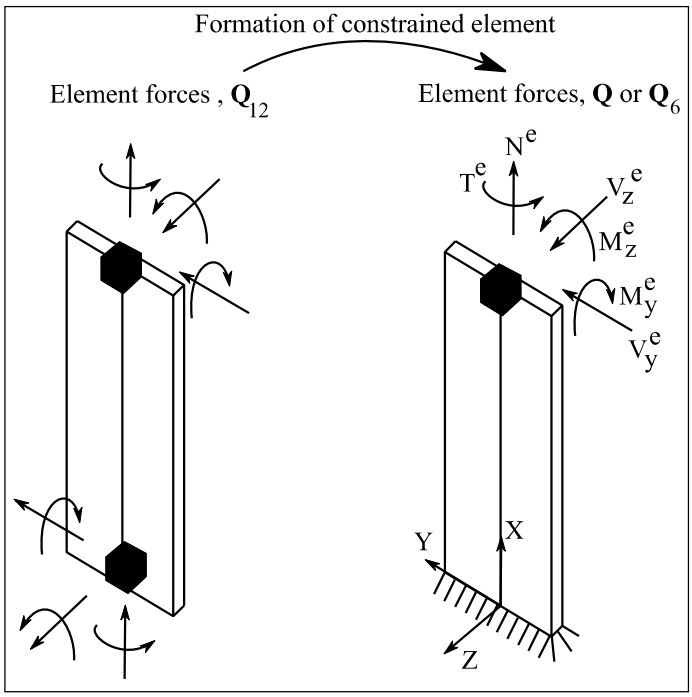

Figure 2-1. Degrees of freedom of the FWE.

In order to calculate the latter integral involved in this flexibility formulation, the element is subdivided into several control sections along its longitudinal axis x, and the Gauss-Lobatto quadrature rule is used. Every section is discretized in inelastic fibers, and the variables depending on x are simply evaluated at the quadrature points and treated like constant values afterwards.

However, as opposed to a displacement based formulation, the element force determination is not straightforward, and an iterative procedure is required. In the compression and bending case, an algorithm that requires one level of iteration has been developed (Spacone et al., 1996). In this thesis, an additional evaluation must be performed to account for shear deformations. The algorithm is schematically shown in Figure 2-2 and goes as follows. Let us start with the known variables from the last iteration that reached convergence, say step i. The variables are the element stiffness matrix $\boldsymbol{K}_i = \boldsymbol{F}_i^{-1}$; the section flexibility matrix $\boldsymbol{f}_i$; the section deformation vector $\boldsymbol{d}_i$;

the corresponding section force vector $\boldsymbol{D}_i$; the element force vector $\boldsymbol{Q}_i$ and the new displacement increment vector $\delta\boldsymbol{q}_i = [\delta u_x \quad \delta\theta_y \quad \delta\theta_z \quad \delta u_y \quad \delta u_z \quad \delta\theta_x]^T$, where $\boldsymbol{u}$ and $\boldsymbol{\theta}$ represent displacement and rotation of the section. The first step of the algorithm (Figure 2-2) is to compute the updated nodal element force $\boldsymbol{Q}_1$ due to the current displacement increment $\delta\boldsymbol{q}_1$, using the last available element stiffness, $\boldsymbol{K}_0$. Once $\boldsymbol{Q}_1$ has been computed, the increment in section forces $\delta\boldsymbol{D}_{j+1}$ is computed by equilibrium using the element force increment $\delta\boldsymbol{Q}_j$ and equilibrium matrix $\boldsymbol{b}$. The increment in section deformations $\delta\boldsymbol{d}_{j+1}$ is evaluated using the flexibility matrix $\boldsymbol{f}_i$ computed in the previous step. By using the section deformations, and under the assumption of plane sections, the strains in each fiber are easily computed. Based on the uniaxial constitutive relationship for concrete and steel, the updated stress $\boldsymbol{\sigma}_{j+1}$ and tangent stiffness $\left(\frac{d\sigma}{d\varepsilon}\right)_{j+1}$ are evaluated. The same procedure is followed for the shear stress and shear stiffness, though additional input variables must be provided (section deformations and forces) as it will be explained later in the document. The algorithm then computes the updated flexibility matrix $\boldsymbol{f}_{j+1}$ and resisting force $\boldsymbol{Dr}_{j+1}$ of the section by integrating the stresses and stiffnesses from each fiber, and by directly using the values from the shear model. Residual or unbalanced forces for the section $\boldsymbol{Du}_{j+1}$, are calculated, which lead to residual element deformations $\boldsymbol{s}_{j+1}$ as a result of integrating the residual section deformations $\left(\boldsymbol{f}_{j+1} \cdot \boldsymbol{Du}_{j+1}\right)$ along the element of length L. The energy error is calculated (Figure 2-2), and if less than the tolerance of 10^{-5} (following the recommendations provided elsewhere (Spacone et al., 1996)), convergence is assumed. Otherwise a new correction in the force increment $-\boldsymbol{K}_{j+1}\boldsymbol{s}_{j+1}$ is applied to the element, and all computations are repeated.

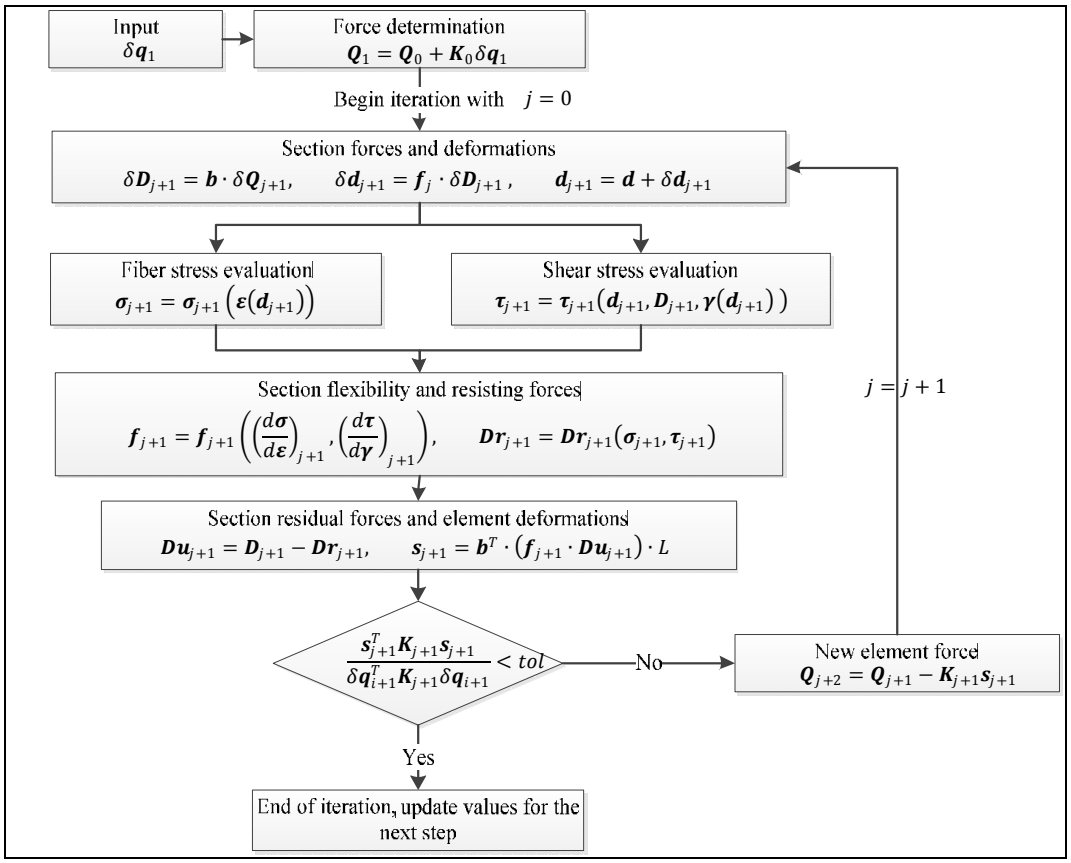

Figure 2-2. Schematic representation of the iteration involved in the FWE algorithm.

Moreover, in order to model strain penetration effects due for instance to bar pull-out and some foundation interaction at the interface between the wall and its foundation, an additional section accounting for these effects was placed in the nearest part to the foundation (Zhao & Sritharan, 2007)**.** However, this model is not very realistic because: 1) the model assumes a plane interface, i.e., slip is proportional to the location of bars; and 2) the strain penetration increases only up to the peak response and after that, the additional section starts unloading because one of the actual sections of the element will soften, and hence the pull-out effect is underestimated from peak resistance point until complete failure.

3. FIBER FORCE-DEFORMATION CONSTITUTIVE MODELS

Steel and concrete fibers are considered in the model. In the case of concrete fibers, the Modified Kent & Park model without tensile strength (B. Scott, Park, & Priestley, 1982) was used, and the unloading-reloading curves were assumed to be straight lines without degradation (Karsan & Jirsa, 1969). The cyclic behavior of the model can be seen in Figure 3-1 where the maximum strength point is $(\varepsilon_0, \sigma_0)$ and the residual strength is $(\varepsilon_r, \sigma_r)$. Concrete fibers are divided into three categories: 1) unconfined fibers; 2) confined fibers; and 3) cover fibers. The first two, have a residual stress $\sigma_r = 0.2\sigma_0$ while cover fibers have no residual stress due to spalling of concrete.

Instead of using in this research the residual deformation ε_r as an input, its value is calculated from the crushing energy associated with the concrete, as it will be explained next. For unconfined concrete, the formula proposed elsewhere (Nakamura & Higai, 2001) is used, and for confined concrete, the energy was extracted from the shape of the concrete force-deformation constitutive relation given earlier in (B. Scott et al., 1982) and (Legeron & Paultre, 2000) —their average was selected. Both energies have referential lengths; for unconfined concrete, reference (Nakamura & Higai, 2001) presented an equation to calculate the fracture length. However for confined concrete, there is no such formula although the fracture length is larger than for plain concrete.

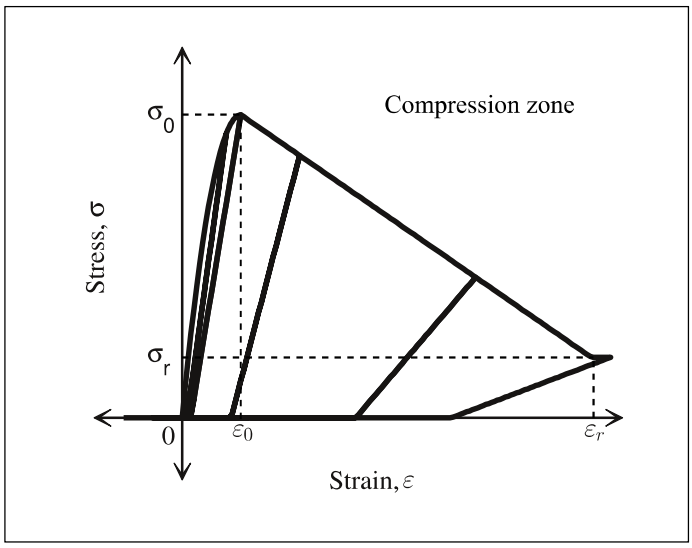

Figure 3-1. Cyclic model of concrete.

Because the number of steel fibers representing the reinforcing bars is much less than the concrete fibers, their model can be substantially more complex without affecting the numerical efficiency of the formulation. The cyclic behavior proposed for steel fibers is presented in Figure 3-2. In this case a path dependent cyclic stress-strain relationship was used for bars. It included buckling (Dhakal & Maekawa, 2002) with corrections in the buckling reload (Suda, Murayama, Ichinomiya, & Shimbo, 1996). This model uses a linear piecewise function to define the backbone curve, and the Menegotto-Pinto model for cyclic behavior. Although the model can effectively reproduce the Bauschinger effect, bar buckling, and bar fracture, it fails to account for fatigue fracture. The behavior also depends entirely on the backbone curve, and hence the buckling starts only when the backbone reaches the buckling point. The same happens for bar fracture.

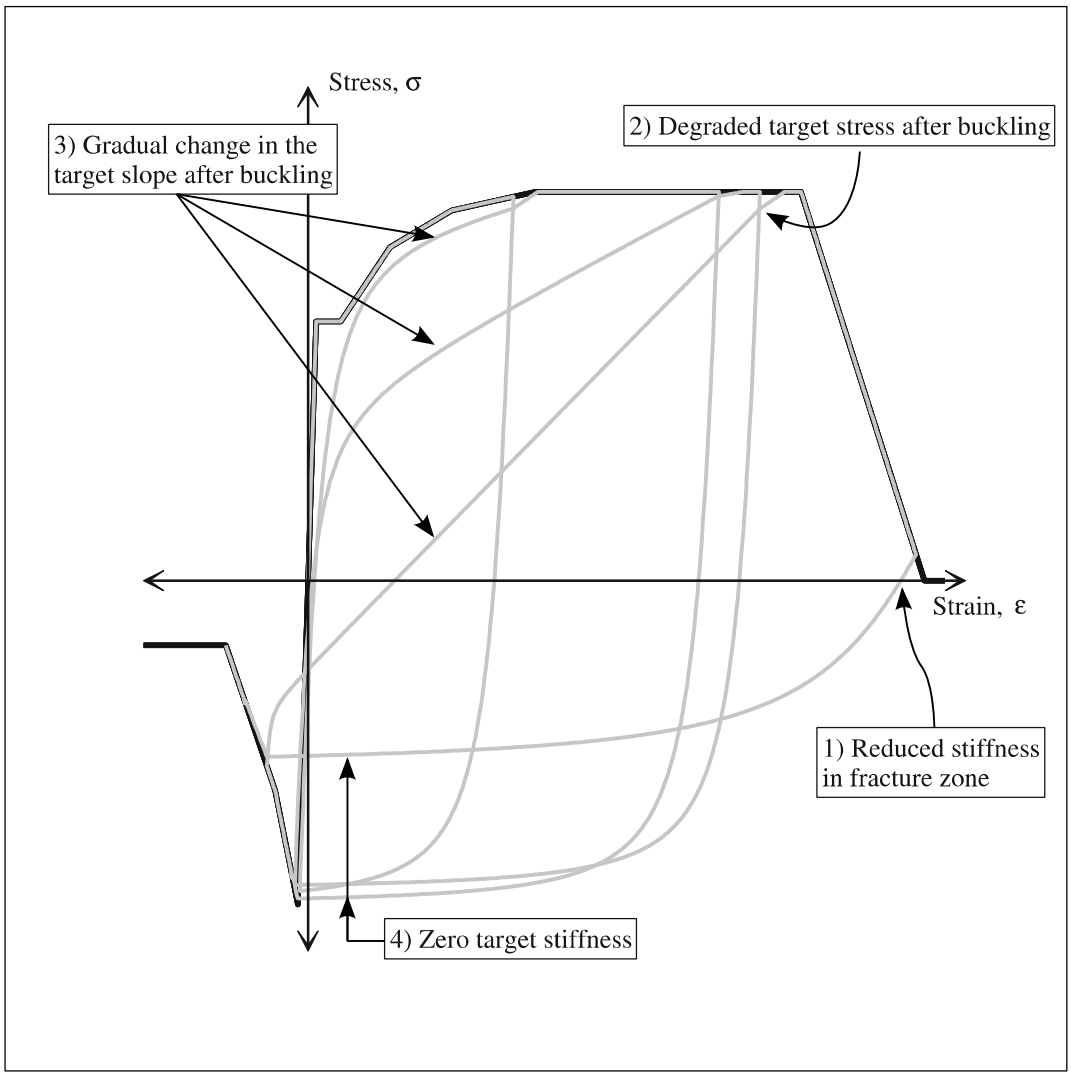

Figure 3-2. Cyclic model of a steel fiber with some changes to improve numerical robustness.

In order to apply the model of steel fibers in a robust way, some modifications are introduced into the model as shown in Figure 3-2. These modifications are defined next. First, as the bar fractures due to high tensile strain—fatigue is not considered—, the backbone curve ends with a linear descending branch of stiffness 10% of the initial stiffness. While unloading in this descending branch follows the rules presented

elsewhere (Dhakal & Maekawa, 2002), unloading slope is reduced proportionally with the stress level as shown in Equation 3:

$$E_u = E_{uDhakal} \times \frac{\sigma(\varepsilon)}{\sigma_{max}} \tag{3}$$

Where $E_{uDhakal}$ is the unloading stiffness—slightly less than the elastic stiffness—and $\sigma(\varepsilon)$ is the current stress and σ_{max} is the maximum historic stress in tension. This modification prevents the overestimation in the energy dissipation of cycles where the unloading stress is close to zero. Second, the degradation after buckling proposed earlier (Suda et al., 1996) was modified to include a soft weighting function that reflects damage as a function of stress corresponding to the buckling reloading point. In the original model, the degradation depends on the number of cycles, parameter that is hard to define when there are partial loading and reloading cycles. Equation 4 shows the arbitrary modification implemented following experimental results (Suda et al., 1996):

$$\begin{aligned} ns &= \frac{\sigma(\varepsilon)}{\sigma_{yield}} \leq 1, \;\; \varepsilon < 0 \\ \sigma_{tgt} &= \min\left(\left(0.18\sqrt{ns} + 0.82\right) \times \sigma(\varepsilon_{max}), \;\; \sigma_{Last\_tgt} \;\right) \end{aligned} \tag{4}$$

Where ns is the current stress normalized by the yield stress; σ_{Last_tgt} is the last positive target stress; σ_{tgt} is the current target stress; ε_{max} is the maximum deformation in the loading history; and the mathematical expression $\left(0.18\sqrt{ns} + 0.82\right)$ is limited to the range $[0.9 \rightarrow 1]$ given the range of ns $[0.2 \rightarrow 1]$, where 0.2 indicates failure because of buckling. The term $\sqrt{ns}$ appearing in Equation 4 was chosen because a linear function or a bigger power, penalizes σ_{tgt} excessively, while the square root makes the term $\left(0.18\sqrt{ns} + 0.82\right)$ close to 1—model without buckling damage—and gets close to 0.9 when the bar is severely buckled. A value 0.9 was used because it corresponds to the value used typically for highly buckled bars without fatigue degradation (Suda et al.,

1996). Third, the model reaches the target stiffness E_{tgt} after buckling proposed elsewhere (Maekawa, Pimanmas, & Okamura, 2003) gradually. Because of the large differences in stiffness it was considered unrealistic to shift suddenly the target stiffness from the point just before buckling to the beginning of buckling. Equation 5 shows the proposed mathematical expressions:

$$fac = \begin{cases} 4.6 - 4.5ns, & ns > 0.8 \\ 1 & ns \leq 0.8 \end{cases}; \; E_{tgt} = fac \times \frac{0.9\left(\sigma_{tgt} - \sigma(\varepsilon)\right)}{\varepsilon_{max} - \varepsilon} \qquad (5)$$

Where fac ranges from 0.2 to 1 and it is the modifier of the target slope. Hence, if the point is near buckling point, $ns \approx 1$, $fac \approx 0.1$, and then, the target stiffness is similar to that of the model without buckling. On the other hand, if $ns < 0.8$, fac equals 1 and the target slope is the one proposed earlier (Maekawa et al., 2003).

The limit of 0.8 for ns in Equation 5, is an arbitrary value that aims to achieve a soft transition in behavior between the stiffness values corresponding to $0.8 \leq ns \leq 1$. And fourth, the target stiffness for the buckling zones is set equal to zero not to cause unrealistic compression in a buckled bar after unloading from very high tensile strain, e.g. 0.01 m/m.

In order to achieve convergence and enforce equilibrium in Newton-Raphson iterations, a choice between secant and tangent stiffnesses was used based on previous literature (Dides, 2003). In summary, this algorithm states that when the slope increases abruptly, the tangent stiffness should be used to enforce equilibrium and, vice versa, when the slope decreases abruptly, the secant stiffness attains equilibrium.

4. MODIFIED REGULARIZATION FOR HIGH AND LOW AXIAL LOADS AND NEARLY CONSTANT MOMENT

4.1 Theoretical background

For an element subjected to uniform compression, all fibers within a section are subjected to the same state of strain and stress and all sections are subjected to the same load. Because a section is composed of concrete and steel fibers which present softening after maximum strength due to crushing or buckling, deformations in the element will tend to localize at the first section of the element reaching such a behavior (the weakest link), while the rest of the sections will unload to preserve the axial equilibrium of the element. This phenomenon is known as localization, and it is experimentally observed when softening materials are used, like concrete and steel in compression (Figure 4-1).

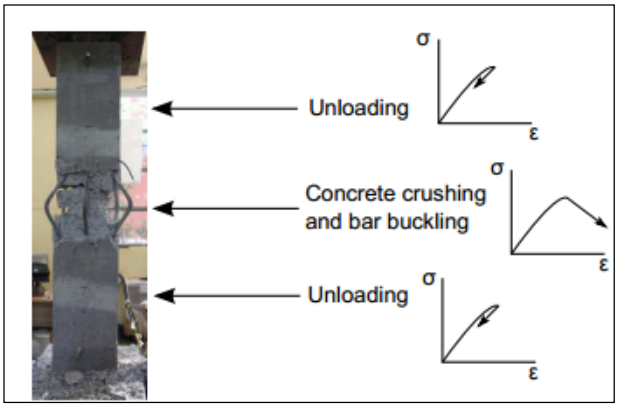

Figure 4-1. Localization under pure axial load (L M Massone, Polanco, & Herrera, 2014)

The numerical manifestation of this localization behavior in flexibility based fiber element models is that the numerical response depends on the number of integration points used to evaluate the response along the element. This is because the number of integration points distributed over the length of the element, L, determines the length

associated with each section, $L_i = w_i L$ (w_i is the weight given from the numerical integration scheme). Therefore, the fracture length where the concrete crushes and bars buckle is one of these L_i lengths. For example, given a stress-strain curve of an elastic material with a softening branch, which ultimate deformation is ε_u at zero stress, the ultimate global deformation δ_u of an element of length L will be the contribution of the unloading zones plus the contribution of the damaged zone, i.e., $\delta_u = \left(\sum_i (L_i \times \varepsilon_{final})\right)_{unload} + \left(\sum_i (L_i \times \varepsilon_{final})\right)_{damage} = \sum_i L_i \times 0 + L_j \varepsilon_u = L_j \varepsilon_u$, which clearly depends on the length associated with the integration point.

In order to make the response of the numerical element objective, two regularization techniques have been proposed for fiber models: (1) to lump the inelasticity at both ends of the element (M. H. Scott & Fenves, 2006) and carry out the integration using the Gauss-Radau scheme that allows to choose the length of the plastic hinge; and (2) to modify the stress-strain relationship of RC fibers by keeping the post-peak energy constant (Coleman & Spacone, 2001), denoted as energy regularization, which enables objective global responses. A well-known drawback of the first method is the difficulty to handle the spread of inelasticity from the element ends, as well as its sensitivity to the plastic hinge length, which is usually unknown a priori.

In theory, energy regularization techniques should not present such problem, and because of their more general application will be used in this investigation. However, energy regularization also has certain shortcomings to achieve exact objective results, or in some particular cases, affect convergence. Based on empirical observations three main situations where such undesirable behavior occurs are: (1) under the presence of extremely high axial loads, say axial load ratios ALR>0.35; (2) under the presence of very low axial loads, say ALR<5%; and (3) in regions of fairly constant bending moment with several integration points. In order to better understand these cases, an explanation for the pure axial case is first provided and followed by the bending-compression case.

Under the assumption of a constant crushing energy, which has been carefully studied earlier (e.g., (Jansen & Shah, 1997; Nakamura & Higai, 2001)), the energy regularization for the pure axial behavior is exact and can be mathematically proven—the same observation is also valid in the case of buckling of a bar. Shown in the plot to the right in Figure 4-2 is the average stress-strain ($\sigma - \varepsilon$) modification required for an element of total length L given the average $\sigma - \varepsilon$ curve for a short sub-element of length L_1 (hatched). The $\sigma - \varepsilon$ curve in the latter consists of a linear inelastic branch followed by a softening branch. Let us now define the fracture energy $G_c = L \cdot \int_{\varepsilon_r}^{\varepsilon_u} \sigma(\varepsilon) d\varepsilon$, which is represented in Figure 4-2 as the grey shaded area under the ($\sigma - \varepsilon$) curve (actually, the shaded area is G_c/L). The constant energy assumption defined by $G_1 = G_0 =$ constant $\equiv G_c$ implies that the grey shaded area under the $\sigma - \varepsilon$ curve is smaller for the longer element ($G_0/L_0 = G_c/L$) relative to the shorter one, i.e., $G_1/L_1 = G_c/L_1 > G_c/L$. Please note that the energy preserved is that after reaching peak strength (shaded area), and not the energy before peak strength as shown by the white area under the $\sigma - \varepsilon$ curve (Figure 4-2). Indeed, in a pure axial behavior after reaching peak strength (ε_0, σ_0), all undamaged sections in series with the damaged ones, unload until they reach the residual deformation ε_r, while the damaged sections go beyond this point along the softening branch of the $\sigma - \varepsilon$ curve. This implies that the pre-peak energy represented by the white area would not be conserved between two elements subjected to the same axial load and one longer than the other. The longer element would release more pre-peak energy than the shorter one, while the shaded energy would be conserved by construction.

In the case of constant bending, or in cases of simultaneous bending and compression, the example of a uniform axial stress state is no longer valid, and the strains increase in the fibers farther away from the rotation axis. Thus, though some fibers at the edge of the section soften first, the section as a whole may still not degrade. This leads to a more complex mix situation of localization, with some non-degrading sections with degrading fibers, which introduces subjectivity into the global response. It is only after reaching

global peak strength that the softening behavior of fibers becomes consistent with that of the sections.

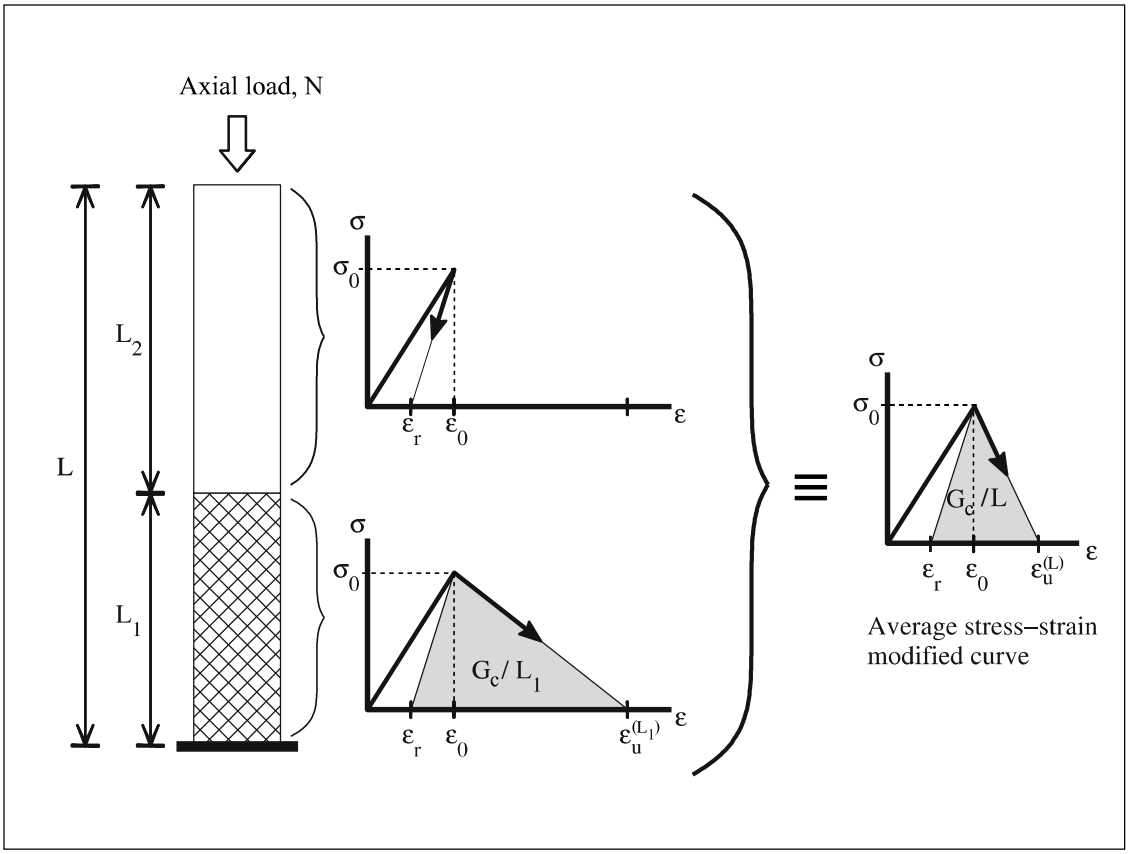

Figure 4-2. Schematic representation of the homogenization (regularization) of the $\sigma - \varepsilon$ curve for an element under uniform axial load; softening branch gets steeper for a longer element.

Schematically shown in Figure 4-3 is a typical lateral pushover analysis curve for a shear wall that presents three distinctive zones in the response: (1) an essentially linear elastic response with neither softening nor yielding, but with cracking in concrete, which is assumed not to affect the response relative to other nonlinearities; (2) an intermediate region with non-localized sections, but with some concrete fiber softening due to high axial loads (shown in black in the element sections), and/or some steel fibers yielding

(shown in grey in the element sections) in one or more sections; and (3) the localization region, characterized by a single section softening, while the rest of the sections and fibers unload. Results presented in Figure 4-3 correspond to the wall section indicated to the right (for further details on the wall, see (Alarcon et al., 2014)) and the $F-\delta$ curve has been presented keeping the right proportions. Furthermore, the cross section showed has a light, medium and dark gray zones representing cover, unconfined and confined concrete respectively. The latter has jagged borders trying to achieve the effective form (Mander, Priestley, & Park, 1988)—a parabola between reinforcing bars (shown inside the encircled zone). The concrete parameters $G_c, \sigma_0, \varepsilon_0$ in the effective confined area inside the boundary bars has been modified so that, $A_{un} \cdot \sigma_0^{(un)} + A_{eff} \cdot \sigma_0^{(eff)} = A_{con} \cdot \sigma_0^{(con)}$ (and the same goes for G_c, ε_0) where "un", "con", and "eff" refers to the unconfined, confined and effectively confined areas. The confined area is the rectangular area inside boundary bars and its parameter are the one explained earlier in this document. The unconfined area is formed by the remaining triangular areas inside boundary bars. For simplicity, the confined area outside boundary bars has been assigned the same effective parameters.

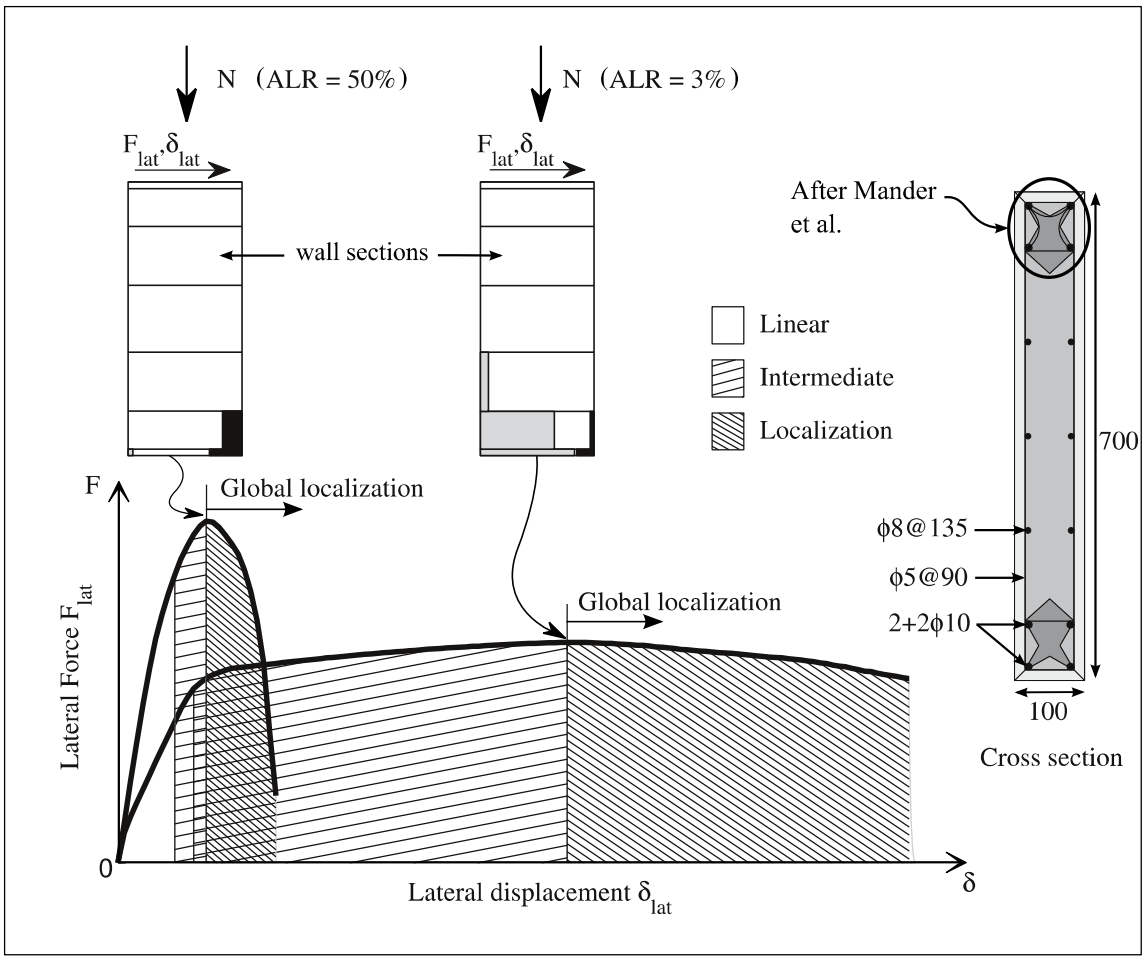

Figure 4-3. Localization behavior zones during a typical pushover (all dimensions in mm)

Interpretation of Figure 4-3 is key in understanding the problem with energy regularization in shear walls, i.e. the spread of inelasticity in the intermediate region before any section softens as a whole does not represent localized behavior. The rationale behind of our proposed procedure does not impose energy regularization in this intermediate zone where there is still non-localized behavior. The existence of an intermediate region implies that extreme fibers would fail in two or more sections, which is consistent with a non-localized behavior. Consequently, the energy regularization should start later, and together with the localized behavior at the section

level. Results in Figure 4-3 qualitatively shows the predicted spreading of inelasticity for high and low axial loads. For high axial loads, fiber crushing tends to spread beyond the localized section, which is a spurious effect introduced by the assumption of plane sections. Because this effect is limited, it can be corrected by the modification explained in the next paragraph. Furthermore, for low axial loads, steel yielding and hardening spread more than concrete crushing or bar buckling, and matches with what is observed in reality. Please note that the worst case scenario for this analysis would be for a constant bending moment, since all the sections will present softening, yielding, and/or hardening of fibers before the response localizes in a single section. Because no method can discriminate what section will start softening, a small perturbation needs to be introduced to artificially weaken slightly a section to avoid numerical problems, say, by reducing the section area in 1/1000th.

The proposed simplified technique to account for the non-localized behavior in the intermediate region aims to find a common strain to all fibers, ε_{reg}, from which the regularization is needed. Fibers will behave as if no localization happens before reaching ε_{reg}, and from there on will be regularized to account for localization. The simplification of using a single ε_{reg} for all fibers can be justified because fibers leading to the problem in this intermediate zone, which are the farthest from the bending axis, are the ones that control the global behavior of the section because their larger contribution to the resisting moment. Essentially, they control the peak strength and failure behavior of the wall section.

In general, for high axial loads, ε_{reg} lies within the softening branch of the $\sigma - \varepsilon$ curve for concrete, while, for low axial loads, ε_{reg} lies within the yielding or hardening zone of the $\sigma - \varepsilon$ curve for steel which will be explained thoroughly in the next paragraph. Figure 4-4 shows an example of the modification of a $\sigma - \varepsilon$ curve for (a) concrete in compression, and (b) steel in tension. In both cases, the $\sigma - \varepsilon$ curves are unique up to ε_{reg}, but from there on, energy regularization takes place as shown by the different slopes for the different element lengths. In case of concrete modification, it usually

improves the quality of the regularization. Thus, as will be shown later, when axial loads are high and/or bending moment is almost constant between sections, the regularization leads to greatly improved results. However, when axial loads are low and the modification is not needed, the response results are essentially the same. The same principle is applicable for accounting for buckling in the $\sigma - \varepsilon$ curve of a steel bar in compression. The same ε_{reg} used for concrete must be used for steel in compression even when the initial portion of the steel constitutive curve doesn't degrade which is seen for cases where the slenderness ratio L/D is small (L stands for the free length of the reinforcing bar and D is its diameter).

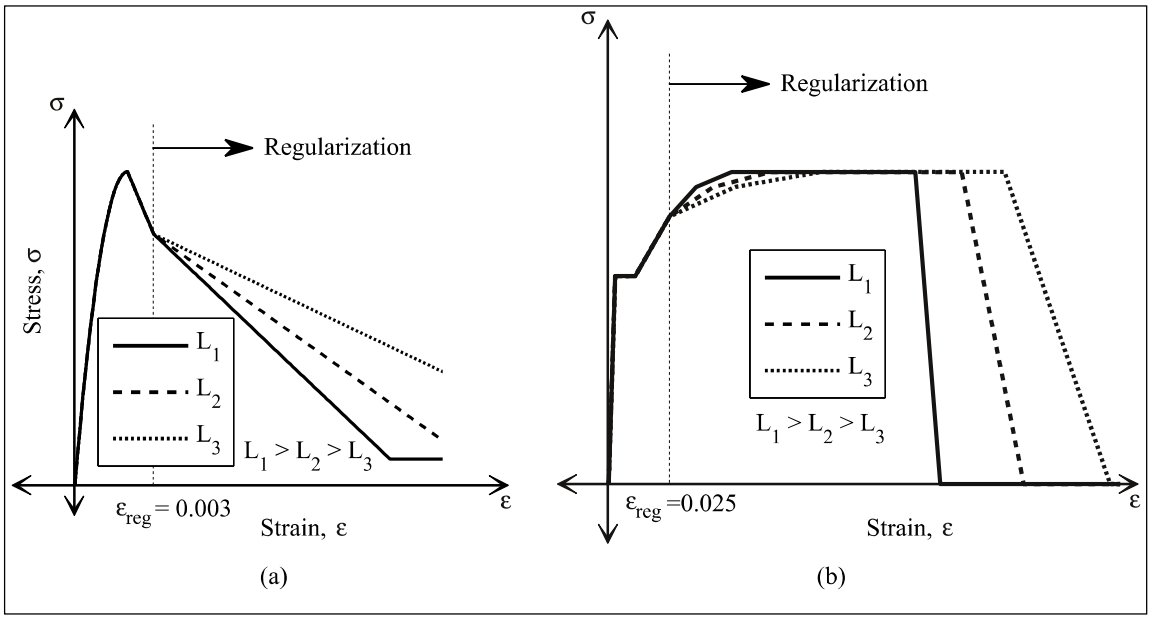

Figure 4-4. Regularization of the $\sigma - \varepsilon$ of RC fibers with fixed behavior up to ε_{reg} for (a) concrete in compression, and (b) steel in tension.

As the $\sigma - \varepsilon$ constitutive curves of RC fibers in compression are modified by the conservation of fracture energy, steel fibers in tension also need to be modified, especially for low axial loads; contrarily, the higher the axial load, the less significant is the effect of this modification. The steel fibers should use the same reference length than

concrete fibers in order to make the response consistent and invariable under the assumption of plane sections. However, there are two issues in doing so: (1) The reference length for concrete of $1300/\sqrt{f_c'}$ (in mm and MPa) established earlier (Nakamura & Higai, 2001) is for plain concrete cylinders and is not necessarily consistent with the plastic hinge length for a wall subjected to bending moment and moreover, the reference length for confined concrete is different from that of unconfined concrete; and (2) the plane sections and perfect bonding would reduce the reference length since under lack of bonding, a larger section of steel could be subjected to the same stress, and hence the actual length that would soften in compression need not match the failure length in tension, i.e., plane section would not apply. For these reasons, the steel reference length is calibrated with values larger than the reference length for concrete, and a heuristically recommended value lies in the range between 25 and 50 cm. This recommendation comes after extensive numerical simulations; a high reference length, or high associated energy, results in a low maximum strength because steel bars require high deformations to reach the hardening zone but in those cases, concrete fibers have already begun to soften. Moreover, for cases of fracture because of high tensile strain (e.g. (Dazio, Beyer, & Bachmann, 2009)), the global lateral displacement of a failing wall, strongly depends on the reference length, therefore, the higher the reference length, the more ductile a wall behaves.

In cases of low ALR, it is common to see yielding and hardening of steel bars within the zone between yield and ultimate moment, which usually involves two or more sections. Deformations localize in a single section when exterior steel fibers harden and exceed in other sections yielding (see spread of grey in sections of Figure 4-3). Therefore, finding ε_{reg} in this well spread behavior is more difficult than for concrete fibers since ε_{reg} spans over a larger range of deformations, i.e. $0 \leq \varepsilon_{reg} \leq 0.06$ (an example can be seen in Figure 4-4(b)), and depends on the axial load. For this reason, even if this method greatly corrects the subjectivity under low constant axial load, it is not recommended for highly varying low axial loads, e.g., ALR ranging from 0 to 10% since it could lead to worse results given by the regularization of the complete $\sigma - \varepsilon$ curve if the fracture

because of high tensile strain is studied. For higher axial loads, there is no such problem, since the spreading of yielding is very limited and the modified regularization for concrete must be used which delivers good results for a big range of ALR (typically ALR from 5% to 40% depending on ε_{reg}).

4.2 Validation of the proposed regularization

In order to validate the proposed regularization, different schemes of regularization, using only one FWE, were compared against each other for two extreme cases of axial loading: (1) high axial load (ALR=34%) with nearly constant bending moment (moment to shear ratio, $M/VL_w = 6$, where M is the bending moment, V is the shear and L_w is the wall width); and (2) very low axial load (ALR= 1%) with $M/VL_w = 3.2$. The two extreme cases are studied under the following regularization assumptions: (a) no regularization by using the original $\sigma - \varepsilon$ curves; (b) energy regularization in the loaded section; (c) energy regularization in all sections; and (d) regularization based on using ε_{reg} in all sections.

The high axial load case was based on the loading condition of a damaged shear wall during the 2010 Maule, Chile earthquake (using the complete section, without accounting for the irregularity, shown later in Figure 6-5(a) and (c)). The element was analyzed using displacement control with constant axial load until static equilibrium is no longer satisfied, which occurs just after the peak strength. Then the pushover curve continues by applying constant axial deformation using the one at last convergence, and incremental steps of lateral deformation. In order to quantify the importance of the regularization of concrete fibers only, steel fibers were assumed elasto-plastic which is indifferent to any regularization. The wall force-deformation results achieved by the proposed regularization schemes can be observed in Figure 4-5.

It is apparent from the figure that schemes (a)-(c) cannot reach in this case a regular overall response, and values after peak response are sensitive to the number of

integration points used. However, the same response using a constant value $\varepsilon_{reg} = 0.00295$ and the regularization scheme proposed enables regularization of the response. Moreover, Figure 4-6 shows analogous results under very low axial load of a U-shaped shear wall introduced later in Figure 6-1 (wall (b)). Again, results of the conventional regularization schemes (a)-(c) lead to inconsistent results with different number of integration points. Differences are very clear in this case of low axial load. The proposed method corrects well this inconsistency by using a fixed $\varepsilon_{reg} = 0.0052$ in this case.

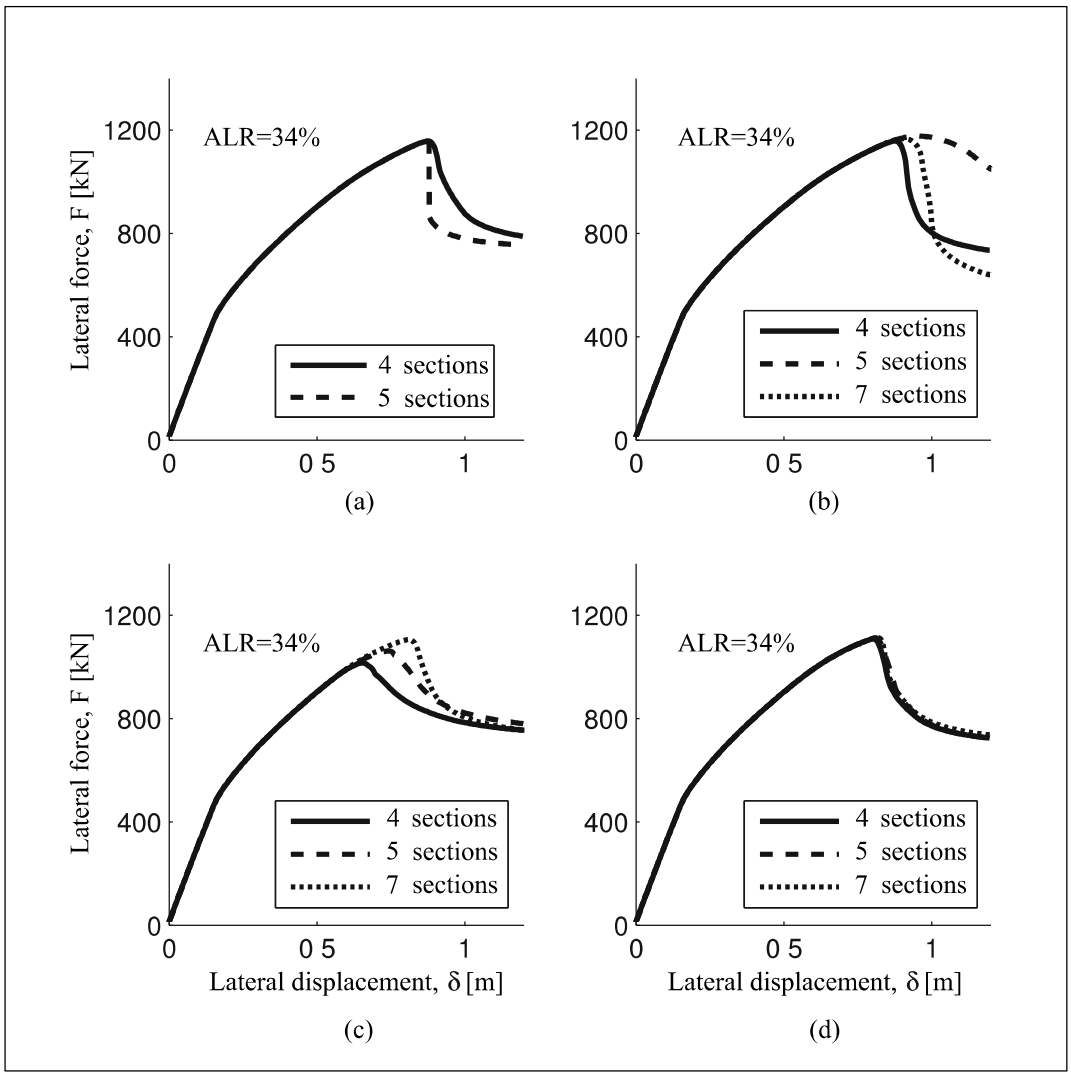

Figure 4-5. Comparison of different regularization schemes and different number of integration points for test shear wall at ALR=34%: (a) without regularization; (b) with regularization in a single section; (c) with regularization in all sections; and (d) with proposed regularization at fixed $\varepsilon_{reg} = 0.00295$.

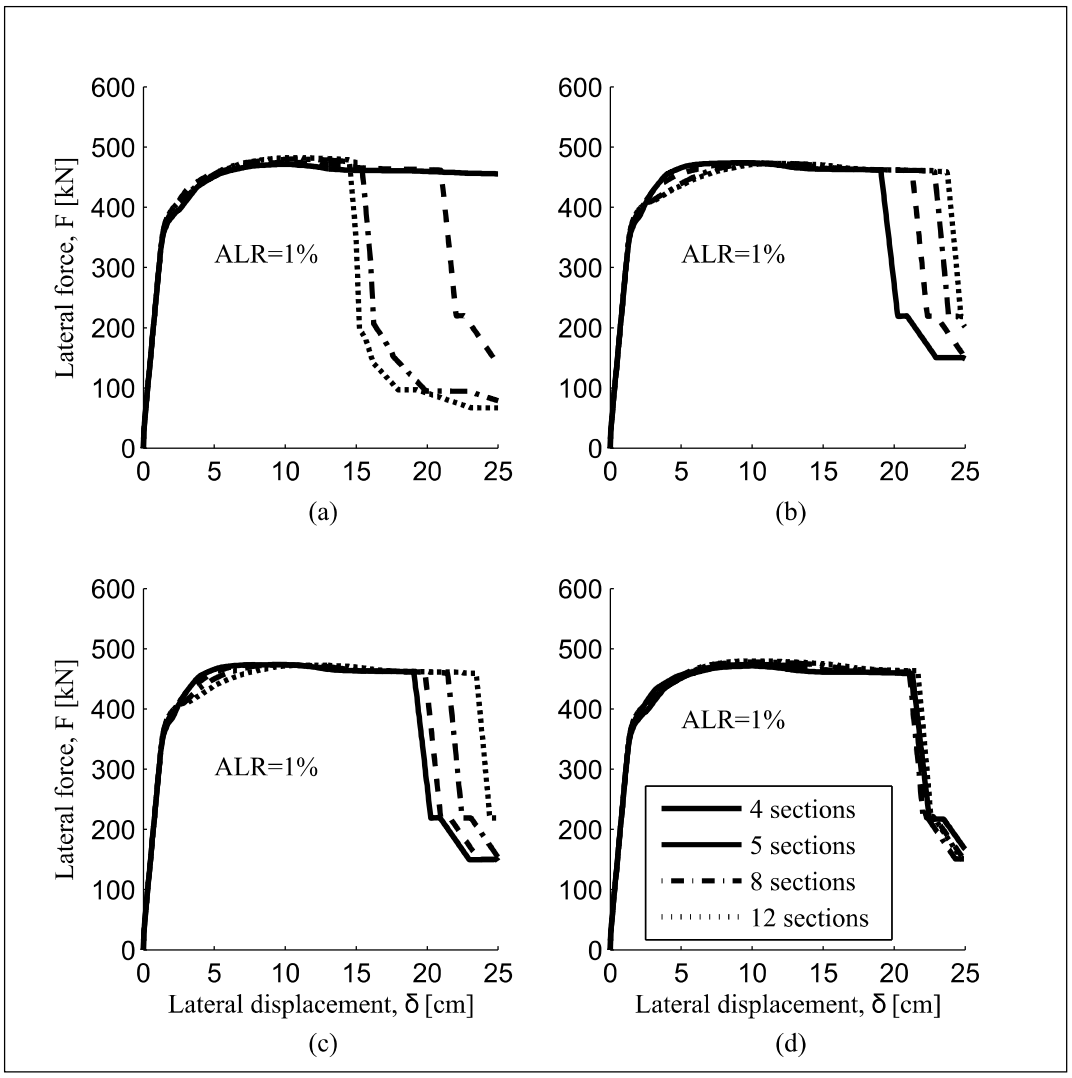

Figure 4-6. Comparison of different regularization schemes and different number of integration points for test shear wall at ALR=1%: (a) without regularization; (b) with regularization in a single section; (c) with regularization in all sections; and (d) with proposed regularization at fixed $\varepsilon_{reg} = 0.052$.

In order for the energy regularization scheme to apply to cyclic behavior, other $\sigma - \varepsilon$ paths and variables need to be modified to achieve an objective response. For concrete, the only possible remaining $\sigma - \varepsilon$ path to modify is the one for the unloading-reloading cycle, which does not need to be modified since it depends on the strain of the unloading

point along the monotonic backbone curve, which is already regularized. However, such is not the case in the reloading situation of a buckled steel fiber, where the reloading slope depends on the stress only. Therefore, for this case the reloading stiffness must be modified by using the same energy principle as shown earlier in Figure 4-2. Something similar happens also with the transition phase between the Menogotto-Pinto cycle and the $\sigma - \varepsilon$ backbone curve from the model used (Dhakal & Maekawa, 2002). The originally proposed length of transition between Menogoto-Pinto cycles and the backbone curve is $5\varepsilon_y$ with ε_y the yield deformation of steel. This length was assumed to change linearly with the length associated with the integration points. Thus for short lengths of integration, where the $\sigma - \varepsilon$ curve is very stretched, the transition phase will be much more than $5\varepsilon_y$, and vice versa.

Please note that ε_{reg} must be calibrated in order for the regularization to take effect over a certain range of axial loads. Moreover, this also depends on the geometric and mechanical characteristics of the studied wall, however, as a recommendation, a good starting point for ε_{reg} in compression, is around $\varepsilon_0 + 0.0005$ for ALR$\approx 10 - 30\%$, and for traction, $\varepsilon_y + 0.02$ for ALR$\approx 1 - 5\%$, where ε_0 is the unit deformation at peak concrete strength and ε_y is the yielding unit strain.

5. SECTION SHEAR MODEL

In the FWE formulation, the flexibility matrix of the section couples the axial and flexural components but shear and torsion remain completely uncoupled at the section level. However element forces become coupled at the element level through the force interpolation matrix b—Timoshenko beam theory—as shown earlier in Equation 2. Several researchers have proposed solutions to the coupling problem of cyclic loading of fiber models. For instance, the fiber method has been integrated with the concrete softened membrane method (CSMM) (R. Mullapudi & Ayoub, 2009), (Li, Li, & Xie, 2011), thus, coupling consistently all effects but requiring more computational effort than a global shear model. Among several types of models, a compilation of strut-and-tie

models to couple shear to the other effects is presented in (Ceresa, Petrini, & Pinho, 2007), which main shortcomings reside on the need for experimental calibration, additional iterations, and lack of experimental validation in some cases. On the other hand, there are efficient ways to account for shear coupling that still lack a theoretical validation (Belmouden & Lestuzzi, 2007) and need to be carefully calibrated due to the use of an elasto-plastic behavior. Also, a model has been developed to couple shear in a displacement based element (Mazars et al., 2006), but it less efficient computationally than the one used earlier (Belmouden & Lestuzzi, 2007).

In order to achieve computational efficiency required for the analysis of a complete 3D building with hundreds of thousands degrees of freedom, a simple 2D global model in each direction is proposed which includes coupling effects incorporated externally. This simple shear model is justified in this case because the walls considered are not short, $M/VL_w > 2$, and the bending-compression behavior is dominated. Regarding the shear uncoupling in the two principal directions, it is justified since for common T-,L- and U-shapes most of the shear is carried by the web of the wall parallel to the direction of elastic shear flow—though this is a very bad approximation for square sections. To improve model consistency, and given that the bending-compression behavior is dominant, the following assumptions are needed in the backbone $\tau - \gamma$ curve (Figure 5-1): 1) the axial force affects the shear behavior, but not viceversa; (2) the point of shear cracking (γ_{cr}, τ_{cr}) is corrected in a very simple way due to bending, and the peak bending strength is transferred in real time to the shear model to identify when the bending-compression behavior triggers failure $(\gamma_{flex}, \tau_{flex})$; (3) the shear reinforcement remains elastic because the bending-compression failure $(\gamma_{flex}, \tau_{flex})$ forces the shear resisting force below the yielding point (γ_y, τ_y); and (4) the critical sections for shear are the same as the critical sections for bending-compression failure.

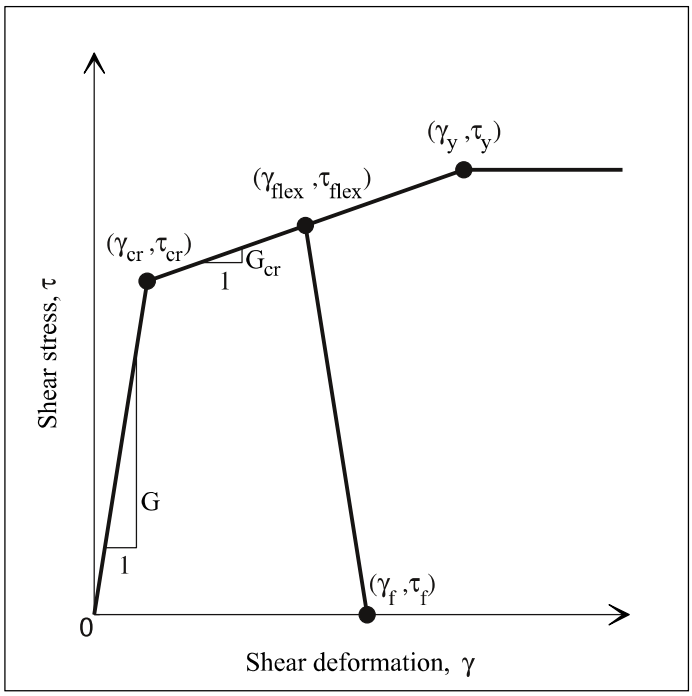

Figure 5-1. Monotonic $\tau - \gamma$ constitutive curve for average stress-strain taking into account bending failure.

The 2D monotonic $\tau - \gamma$ constitutive relation for average shear stresses and shear deformations is based on a simplified model (Gérin & Adebar, 2009) for elements subjected to shear without bending. Therefore, in principle, the shear failure mechanism behind this model is different from the one considered here, which is driven by bending. A typical macro model with no failure consists of two points (Figure 5-1): the cracking point (γ_{cr}, τ_{cr}) and the yielding point (γ_y, τ_y), or equivalently, the peak shear strength. However in a bending-compression dominant behavior, the yielding point in this curve is not reached, and failure begins at $(\gamma_{flex}, \tau_{flex})$. After that, the section is assumed to degrade until it reaches complete failure (γ_f, τ_f). The initial section stiffness is the classic elastic one, say $G = 0.4E$, and the cracked stiffness, G_{cr}, is estimated using the Modified Compression Field Theory (MCFT) (Vecchio & Collins, 1986) assuming that there is no shear-flexure interaction, and that the longitudinal reinforcement is uniformly

distributed over the shear area, which is a reasonable assumption in practice. Following the ACI recommendation, the shear section area is 5/6 of the gross area for rectangular sections, and corresponds to the section of the wall parallel to the loading direction of T and U shaped walls. Therefore, for typical wall sections, the shear area will always be rectangular. The cracked stress τ_{cr} is obtained from the expression for columns in the ACI provisions (ACI Committee 318, 2005), where the cracking stress depends on the average axial stress P/A_g and f_c' as provided by Equation 6.

$$\tau_{cr} = 0.17\left(1 - \frac{P}{14A_g}\right)\sqrt{f_c'} \quad , \qquad P/A_g, f_c' \; in \; MPa \tag{6}$$

This formula was found adequate because: (1) it does not overestimate the axial effect on shear resistance (MacGregor & Hanson, 1969); and (2) the shear resisted by concrete, which corresponds to the shear cracking stress without axial load, takes into account bending when subjected to shear—the cracking stress is overestimated if no bending is considered.

For cyclic behavior, a simple secant path has been adopted, as proposed earlier (Gérin & Adebar, 2009) which allows axial load variations from step to step. Other multi-purpose shear macro models like Takeda and SINA (Saiidi & Sozen, 1979) impose several rules before yielding (considering the cyclic paths), and for each of these rules, an assumption is made as the axial load varies. In the secant model, just a few physically meaningful assumptions are needed (Figure 5-2). Please note that even if the actual walls show pinching (Beyer, Dazio, & Priestley, 2012; Leonardo M Massone & Wallace, 2004), such effect cannot be predicted by the MCFT assumptions under a non-yielding situation.

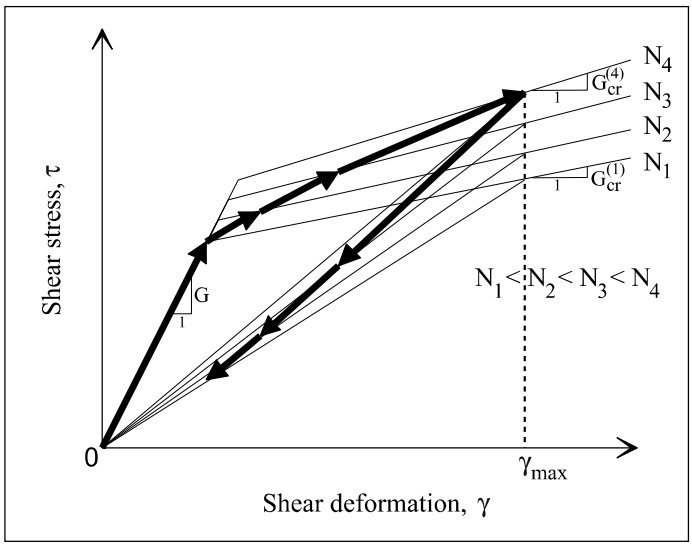

Figure 5-2. Shear backbone $\tau - \gamma$ curve with loading and unloading path for variable axial load.

As axial load varies in Figure 5-2, which is a common case under cycles due to earthquakes, shear resistance is affected, and for high axial loads, one gets larger shear strength, and vice versa. To implement this effect, the backbone curve was described as a function of the axial load by using the MCFT, and hence, there is one backbone curve for each different axial load. The concept of multiple backbone curves is shown in Figure 5-2, and the cracked slopes G_{cr} as a function of the current axial load N are evaluated at each step with an algebraic expression derived with the following algorithm: (1) calculate the $\tau - \gamma$ curve by using the MCFT under an axial load N^*; (2) identify the cracked zone and compute its slope $G_{cr}(N^*)$ by means of a linear regression; (3) Repeat (1) and (2) for different values of axial loads; and (4) calculate the cracked slope as a function of any axial load P by using a linear regression on the data accumulated by repetitions of step (2). Please note that all this numerical computations are calculated just once, at the beginning of the analysis. The schematic cycle shown in Figure 5-2, consists of an increasing value of γ along with an increasing axial load (from

N_1 to N_4) followed by unloading with a reduction of axial load and shear deformations. As presented earlier in

Figure 2-2, before entering the $\tau - \gamma$ constitutive law of shear, at the current j^{th} integration sub-step, an axial load (from $\boldsymbol{D}_{j+1}$) and a shear deformation (from $\boldsymbol{d}_{j+1}$) have already being estimated, so the proposed shear coupling method evaluates the current shear stress $\boldsymbol{\tau}_{j+1}\left(\boldsymbol{d}_{j+1}, \boldsymbol{D}_{j+1}, \gamma\left(\boldsymbol{d}_{j+1}\right)\right)$ on the right curve given by the estimated axial load, and the secant slope $\left(\frac{d\tau}{d\gamma}\right)_{j+1} = \left(\tau_{j+1}^{(i+1)} - \tau^{(i)}\right) / \left(\gamma_{j+1}^{(i+1)} - \gamma^{(i)}\right)$, where i refers to the integration step. This assumes that there is neither degradation of resistance nor stiffness. The only point where the tangent stiffness could be used, depending on the rules proposed elsewhere (Dides, 2003), is at the origin, during transition from unloading to reloading. The only path yet to be explained is the softening branch, and its consequences.

The softening branch of the shear model (Figure 5-1) is difficult to define because it requires a complex analysis of the complete coupled problem, or otherwise experimental data on shear deformations as the element softens. Consequently a slope equal to the elastic one, but opposite in sign, has been assumed independent of the axial load for a square element with the same shear section for each direction and length equal to its width, i.e., a geometric slenderness ratio of 1. This is equivalent to state that the failure of the square element is brittle for all axial loads, but not brittle enough to produce a snap back. A geometric slenderness ratio of 1 was chosen for simplicity to represent the diagonal struts that would match that of the element if the crack angle was 45°—angle formed under no axial load. The selection of slope choice is justified because of the low sensitivity of this slope in the global response of elements dominated by flexo-compression as shown later in Figure 6-4. Moreover, more than 80% of the lateral deformation in our case studies—$M/VL_w > 2$— is due to bending as it has been reported earlier (Beyer et al., 2012). This could make the model simpler, because one could be tempted to follow an unloading path in the shear model after peak resistance instead of following a softening path, however, this would blind the analyst regarding

shear deformations after peak strength, and if these deformations happen to be around 20% the analyst would be completely underestimating shear deformations and hence the global ductility of the wall would be reduced since all that 20% should be taken into account by flexural deformations.

Because the shear behavior shows a degrading zone localized at the most loaded section, the global response depends on the number of integration points as it was shown earlier in this document for the element without shear deformations. In other words, the energy associated with the softening slope just discussed has to be distributed over the length of the element, in order for the global response to be objective. Thus, the slope was as befeore energy-regularized, but in this case, calculations are a bit cumbersome since the unloading slopes of the non-failing sections are not straight lines due to variability of the axial load (Figure 5-3). Shown in Figure 5-3 is a schematic $\tau - \gamma$ constitutive relation with definition of the softening and unloading paths for the case of variable axial load. Stresses increase to reach maximum strength, and then decrease toward the origin, or through a descending branch modified to make the response objective given the initial assumed slope for the square element.

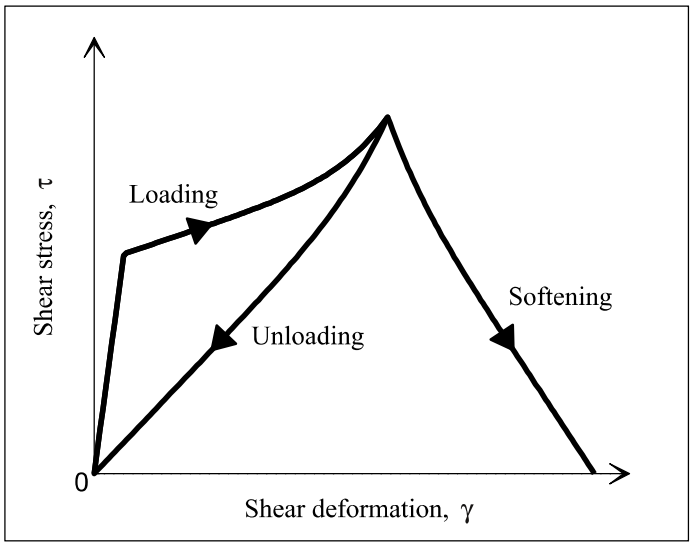

Figure 5-3. Regularized softening branch under variable axial load.

Finally, in order to numerically stabilize and make more robust the inelastic analyses, the possible $\tau - \gamma$ loading and unloading paths between the different backbone curves need to be restrained as shown in Figure 5-4. This happens in situations near the onset of softening, where the increase in shear deformation is very small or even negative in the sub-iterations and the axial load increases. To avoid these undesirable situations, the possible slopes where limited to the range $[0 - G]$ when loading and to $[G_{cr} - G]$ when unloading. This means that if the path is modified, the original equilibrium is not achieved because the actual axial load increment has to be partially applied in the current step in order to keep the path inside the shaded region shown in Figure 5-4. This heuristic criterion has very low effect in real applications because, as it was mentioned before, it generally happens in the vicinity of the maximum lateral strength only.

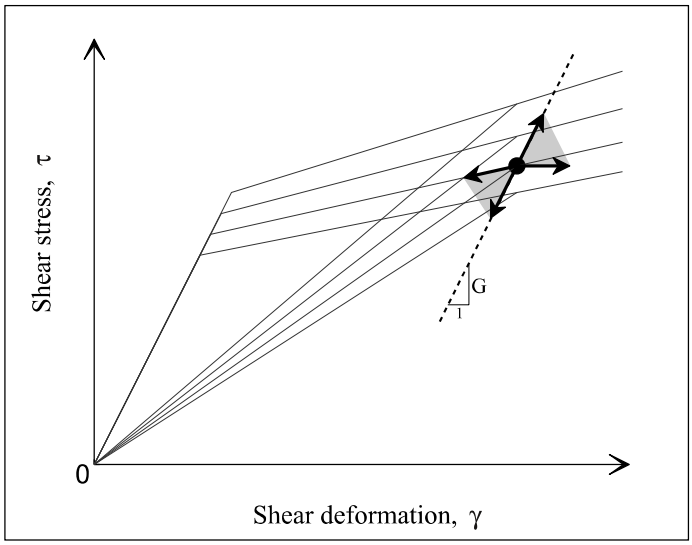

Figure 5-4. Qualitative description of the allowable paths for loading and unloading conditions.

6. VALIDATION WITH EXPERIMENTAL DATA

In this section proposed model is tested using four different wall configurations and only one FWE. The first three tests compare analytical and experimental results of cyclic tests aimed to validate the inelastic behavior of fibers together with the shear and strain penetration models for three different wall shapes. The fourth test aims to reproduce the damage observed in several walls of a building after the 2010, Chile earthquake. The geometry of the first three walls is presented in Figure 6-1 and the fourth's is presented in Figure 6-5(a).

6.1 Validation with laboratory experiments

The studied walls are denoted as WSH2 for the rectangular wall, USW1 for the U shaped-wall, NTW1 for the T shaped-wall and WL for the L shaped-wall. Some of their general geometric characteristics are summarized in Table 6-1 and Table 6-2. The variables are self-explanatory but f_c' is the cylindrical strength of plain concrete; f_{cc_Z}' is the strength of concrete in confined zones along the local Z axis (Figure 6-1); and f_{cc_Y}' is the strength of concrete in confined zones along the local Y axis. Note that in the case of USW1, the confined concrete zone in corners was labeled as Z. The same nomenclature applies for the crushing energy G_c, G_{cc}. The computation of these energies and more detail in fibers used can be seen in appendix A.

Table 6-1. Geometric characteristics and axial load of the sample walls.

Wall	Thickness [cm]	Area $[m^2]$	ALR [%]	Shear span [m]	Loading
WSH2	15	0.300	5.70	4.56	2D
USW1	25	0.875	10.00	3.90	2D
NTW1	15.25	0.602	2.75	7.93	3D
WL	17	1.170	33.00 ± 13.00	3.38	2D

Table 6-2. Mechanical properties of walls.

Wall	f_c' [MPa]	f_{cc_Z}' [MPa]	f_{cc_Y}' [MPa]	G_c [MPa-m]	G_{cc_Z} [MPa-m]	G_{cc_Y} [MPa-m]
WSH2	40.50	-	47.8	0.056	-	0.323
USW1	23.73	31.87	33.0	0.043	0.314	0.332
NTW1	50.00	60.42	63.4	0.062	0.526	0.730
WL	20.00	-	-	0.039	-	-

The studied walls were chosen among plenty of available specimens in the literature in order to show the inelastic capacity of the model to represent buckling and fracture of bars and concrete crushing under 2D and 3D loading conditions. The first wall is a rectangular specimen (WSH2) tested earlier (Dazio et al., 2009), it was selected among the 6 wall specimens tested by the authors mainly because several bars ruptured in tension. In order to reproduce some of the experimental failures, the steel reference length had to be calibrated to 0.45m, and the ultimate strain, ε_{us}, used for the steel was the one from LVDT measurements (Dazio et al., 2009). Furthermore, the length of the element was shortened to 4.4m from 4.56m, since its failure happened about 0.17m above the base—this was not the case other walls from the same authors. The second wall considered for validation was a U-shaped wall (USW1) tested earlier (Pegon, Plumier, Pinto, Molina, Gonzalez, Colombo, et al., 2000; Pegon, Plumier, Pinto, Molina, Gonzalez, Tognoli, et al., 2000). One of the main features of this wall was that the stirrups within the confined area were spaced enough vertically to cause a notorious buckling between two adjacent stirrups ($L/D = 7.5$). No parameter of our model was calibrated in this case. The third wall was a T-shaped (NTW1) element that was subjected to simultaneous biaxial lateral loads. Unlike the U-shaped wall, stirrups were closely spaced (ϕ6.4 @50 mm and L/D≈ 3) which slowed the onset of buckling. This wall was selected to test the hypothesis of plane sections in an unfavorable case because of the long flange (Figure 6-1) which produces the well-known shear lag phenomenon (Hassan & El-Tawil, 2003) as the flange is in tension, and causes the section not to remain plane.

Shown in Figure 6-2 is a comparison between the experimental behavior in the Y-direction and the predicted behavior using the proposed model. Letters (a), (b), and (c) correspond to the WSH2, USW1, NTW1 specimens of Figure 6-1. The first row of plots shows the full inelastic behavior; the second row includes three different conditions, no fracture for WSH2, without reduced buckling slope for USW1, and 2D-loading for NTW1; the third row of plots checks on the relevance of the shear deformations and strain penetration effects.

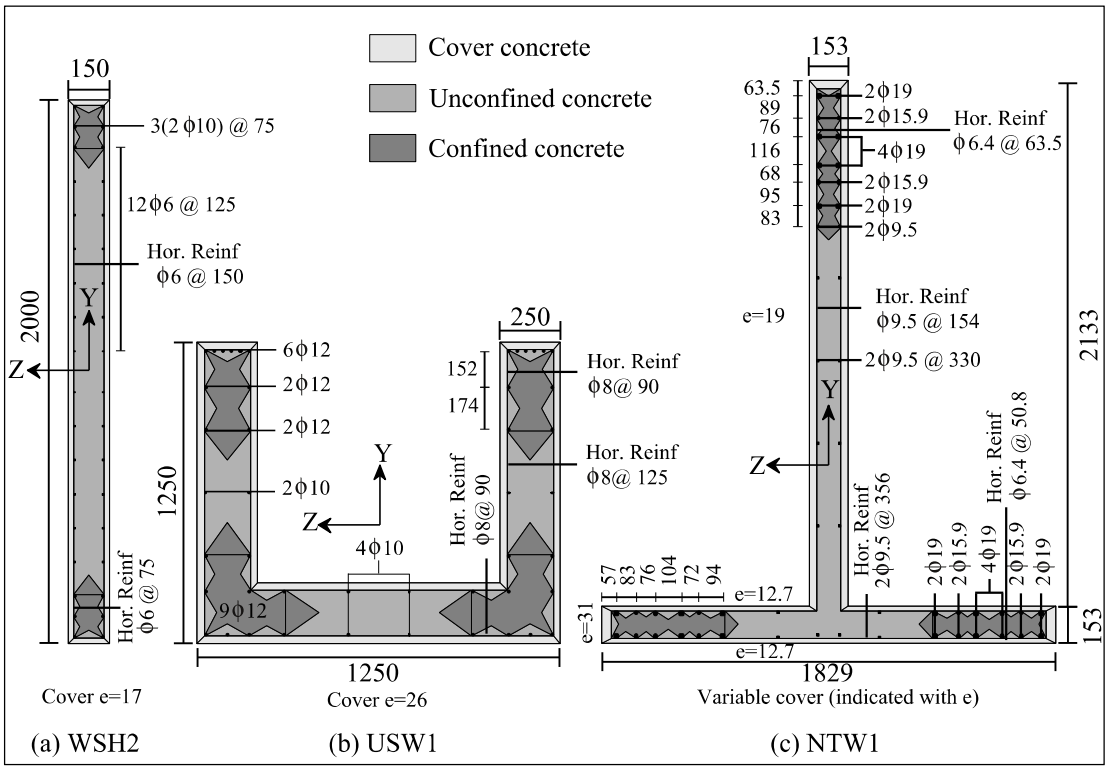

Figure 6-1. Experimentally tested wall shapes used to validate the proposed model: (a) WSH2 (Dazio et al., 2009); (b) USW1 (Pegon, Plumier, Pinto, Molina, Gonzalez, Tognoli, et al., 2000); (c) NTW1 (Brueggen, 2009)

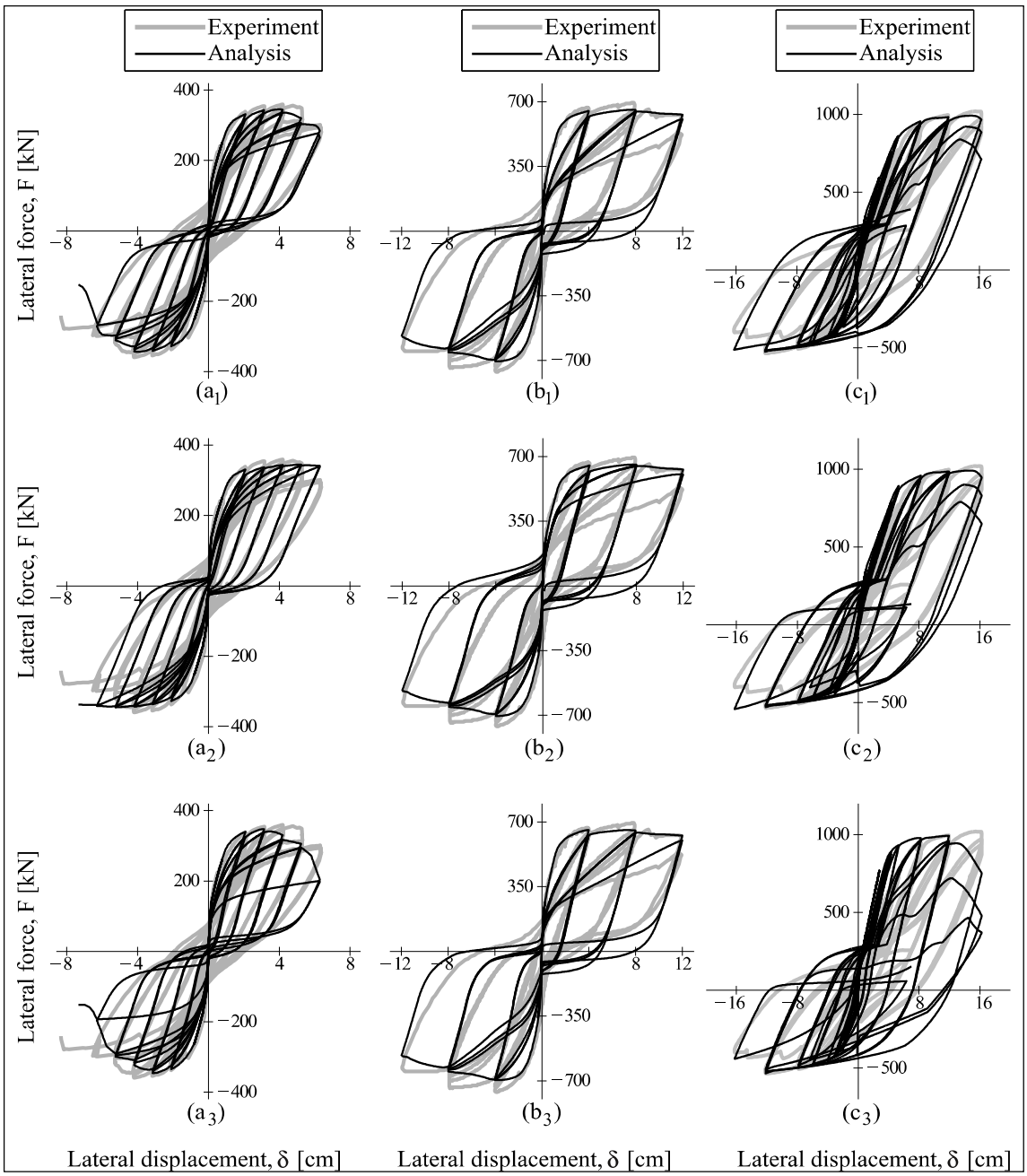

Figure 6-2. Comparison between the analytical and experimental lateral response of the (a) WSH2, (b) USW1, and(c) NTW1 wall specimens subjected to the following assumptions: (a1),(b1), and (c1), complete inelastic model; (a2) without fracture of bars in tension, (b2) without buckling of bars in compression, and (c2) 2D-loading of the wall; and (a3),(b3), and (c3), specimens without shear deformations and strain penetration.

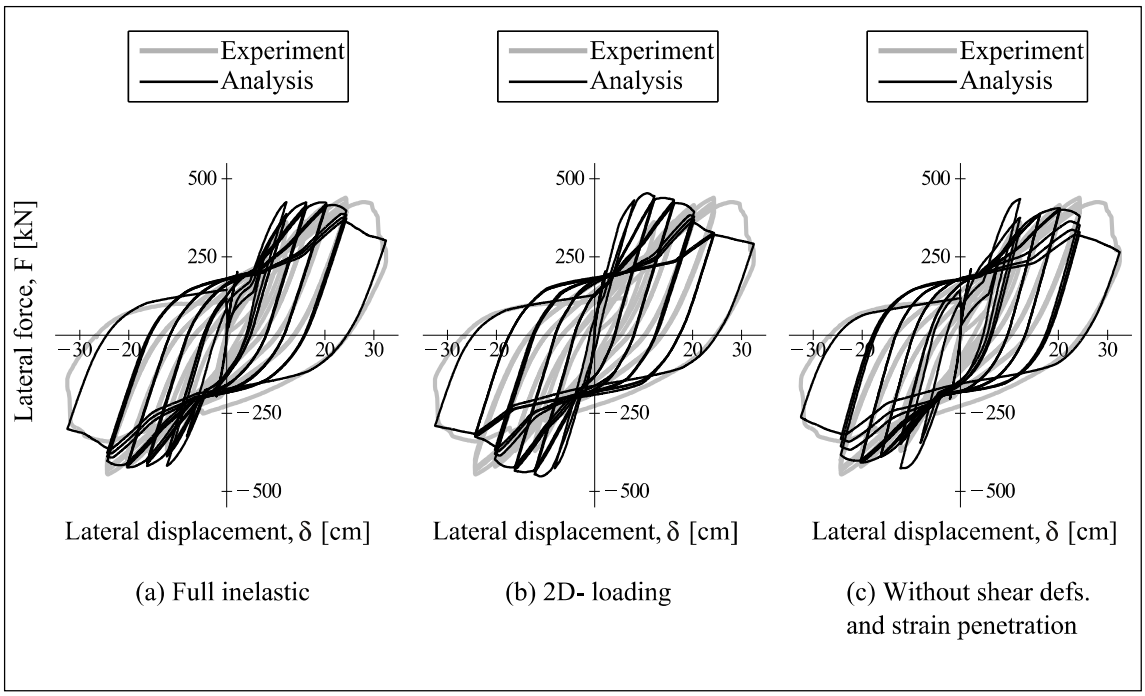

Figure 6-3. Comparison of the lateral response between the predicted and experimental model for the NTW1 specimen and three modeling assumptions: (a) full inelastic; (b) 2D-loading; and (c) without shear deformations and strain penetration.

As shown by the results of Figure 6-2, aspects such as buckling and fracture of a bar, strain penetration, shear deformations, and loading conditions are essential to reproduce the actual behavior in tested wall specimens. For the case of full inelastic behavior identified by subindex (1), results of loading and reloading stiffnesses, wall ductility, and maximum strength are well captured by the model. In the second row of plots, a selected inelastic behavior has been chosen (subindex (2)). For instance, when the fracture of a bar is not modeled (a1), the drop in resistance of later cycles cannot be reproduced correctly by the model; analogously, when the buckling behavior does not account for the reduced slope as proposed elsewhere (Suda et al., 1996), the analysis overestimates the released energy and the reloading slopes in the USW1 wall are far from reality; also for the NTW1 element, if the section is loaded in the Y-direction (c_2),

there are no major differences in the local Y-direction. That is not the case for the Z-direction as shown in Figure 6-3.The third row of plots shows the analyses with no shear deformation and no penetration effects. They show low ductility in general, and they tend to fail sooner than the actual observed behavior.

Although several inelastic behaviors have been included in the proposed model, there are still some differences between the experimental and analytical results. The most relevant are: (1) a marked pinching effect shown by the WSH2 and USW1 models, which is mainly due to the assumption of plane sections because all the concrete in tension to one side of the neutral axis begins to resist compressive stress as the section moment changes in sign; (2) some differences in the last reloading cycles of the USW1 and NTW1 walls due to the fracture of bars after intensive buckling which is not taken into account by the model since the steel depends entirely on the backbone curve and cannot fracture in the middle of a cycle; and (3) predicted cycles in the NTW1 wall tend to release more energy than the observed in the experiment while testing, which is again due to the plane section assumption and also, due to the fixed buckling length in the model. First, the whole prediction could have been less accurate due to the shear lag effect—neglected by assumption of plane sections—and second, the buckling length in the model was set as the spacing between stirrups, while in the experiment, at earlier stages, bars behaved as if a short buckling length was used (probably close to the one chosen), however when the buckling occurred in late cycles the “actual buckling length” was much larger because the core concrete was completely crushed and the wall buckled as a whole.

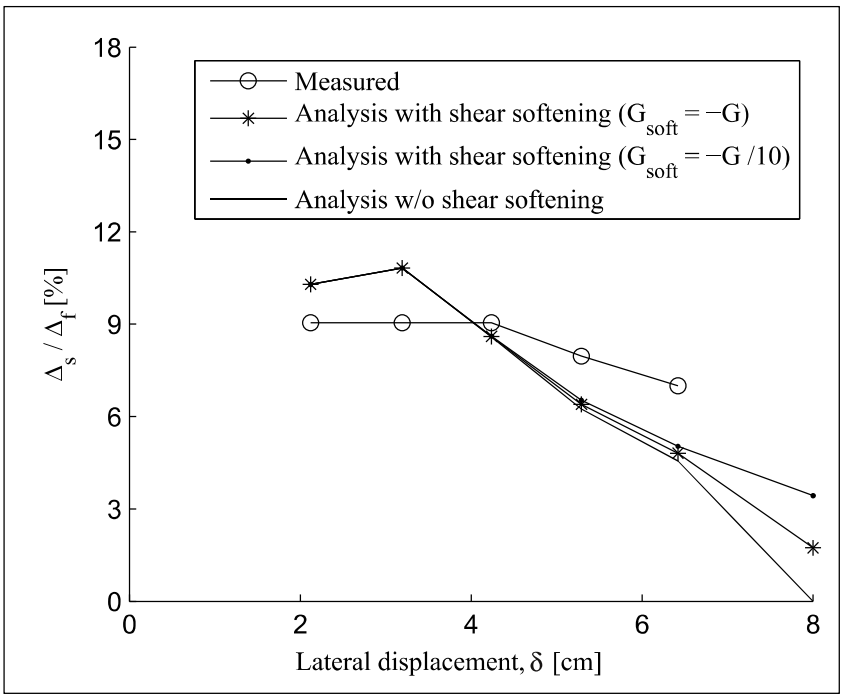

Figure 6-4. Ratio of shear to flexural displacements at the peaks for WSH2.

Although the shear model is very simple relative to the fiber model, it can predict reasonably well the observed shear deformations as shown in Figure 6-4. Given that the walls studied have an aspect ratio larger than 2, shear deformations are a small proportion of the global deformation, thus making the eventual shear model errors less significant. Indeed Figure 6-4 shows the comparison between real and predicted measured ratios of shear to flexural displacements including strain penetration effects for the rectangular wall, WSH2. All models are very similar and the maximum error was 31% relative to the experimental behavior with $G_{soft} = -G$, found in the last cycle at δ= 6cm. The overestimation at the peaks of the first cycles is probably due to the uncertainty in the cracking point and the cracking extension over the length of the specimens; in the model, the cracked stress provided by Equation 5 was possibly smaller than the actual cracking stress, which caused higher cracked shear deformations, and

moreover, this cracked behavior spread over the entire length, while in the experiments, the cracking behavior not always reaches the zone of small bending moment due to shear-bending interaction. The underestimation in the final cycles is probably due to the close interrelation between shear and bending which is neglected by the model, and the lack of damage caused by repetitive cycles assumed in the model. To reflect the maximum differences between analyses, the displacement $\delta = 8$cm was chosen to show the actual percentage values predicted by the shear model with different softening slopes at complete failure. This means, that for the model without shear softening, the residual ratio of shear to flexural displacement is zero at complete failure, while for two other models is between 2% and 5%. This reflects the low sensitivity of the shear softening behavior as stated earlier. A decrease in the softening slope of one order of magnitude results in just twice the shear deformation at complete failure.

6.2 Damage reproduction of a real RC building

A question arises if the FWE would be capable of reproducing or anticipating damage in real shear wall structures. Let us consider the wall shown in Figure 6-5(a), an irregular L-shaped shear wall that suffered severe damage during the 2010, Chile earthquake. The wall was analyzed statically along the Z axis with sufficient length to avoid diagonal cracks ($M/VL_w = 6$), which were not present after visual inspection of the damaged building. Moreover, the presence of a beam which transforms into a wall in the upper stories, shown in Figure 6-5 (b), was considered in the model by modifying the size of the wall sections around that zone.

To calculate the size of each section in the irregularity zone just mentioned, a linear elastic frame element with variable section was analyzed in Sap2000 and calibrated against the response obtained from shell elements using the same software. The analysis consisted of a lateral force at the bottom of the model of the studied wall (Figure 6-5(c)). The result of this calibration was that the width of the frame element has to form a 25° straight line from the beginning of the irregularity as shown in Figure 6-5(c). The

inclusion of the rigid bar in the position shown was done in order to replicate the trapezoidal moment distribution from linear analyses of the building, which is consistent with the location of damage—in the zone with the highest bending moment.

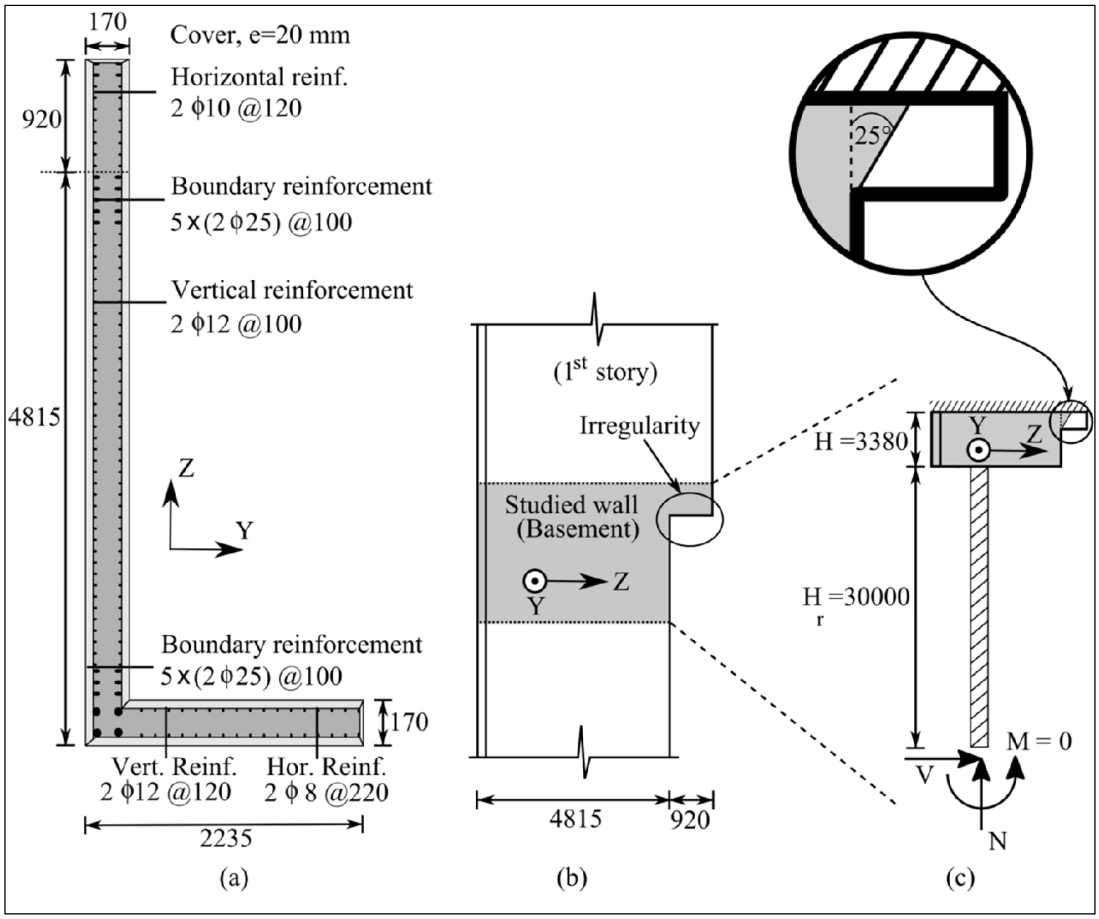

Figure 6-5. Description of wall WL: (a) detailing of the section, (b) schematic elevation inside building and (c) model of the studied zone.

Table 6-3. Loading steps for WL

Step	Direction of δ_{lat}^{top}	Axial Load, N	Axial deformation, δ_a
(0)	Free	$0 \rightarrow 1.4N_0$	Free
(1)	Loading (+)	$1.4N_0$	Free
(2)	Loading (+)	Free	The last from Step (2)
(3)	Unloading (-)	N_0	Free
(4)	Free	$N_0 \rightarrow 0.6N_0$	Free
(5)	Loading (-)	$0.6N_0$	Free
(6)	Loading (-)	Free	The last from Step (5)

In order to make a more realistic analysis, instead of carrying out two different pushover analyses with constant axial load, the shear wall was subjected to half a cycle taking into account different axial loads derived from linear elastic modal analysis. Table 6-3 shows the load history of shear wall WL (Table 6-1and Table 6-2) which is divided into 7 steps denoted as (0) to (6), all of them constrained to have zero bending moment at the bottom of the rigid bar. The variables controlled in the half cycle analysis were: (1) top lateral displacement, δ_{lat}^{top}; (2) Axial load, N; and (3) Axial deformation, δ_a. Before the applying of any lateral displacement, an axial load was applied (steps (0) and (4)) to simulate the effect on the axial load because of the earthquake. These loads, $1.4N_0$ and $0.6N_0$, were the maximum and minimum axial loads extracted from elastic modal analysis using typical load combinations ((INN), 2010). Although these limits come from linear analyses, an error in their magnitude is accepted since the major factor to evaluate in this case is the geometric irregularity. For the two directions, loading was applied in two steps: first, with axial load fixed ((1) and (5)); and second, with axial deformation fixed ((2) and (6)). This separation in two steps was because after reaching peak strength in one direction, static equilibrium is not possible if lateral deformation continues to increase (snapback behavior), or in other words, the wall would start to accelerate.

Shown in Figure 6-6 are the force-deformation results from the half cycle analysis described above. (a) shows the axial load, N, as a function of lateral deformation, δ, measured at the at the top of the studied wall—3.38m above ground— and (b) shows the lateral force, F, versus δ.

One of the key features of the analysis is that the wall is forced to fail, as seen in steps (2) and (6) (Figure 6-6) where the axial load drops because the wall cannot longer withstand the initial axial load.

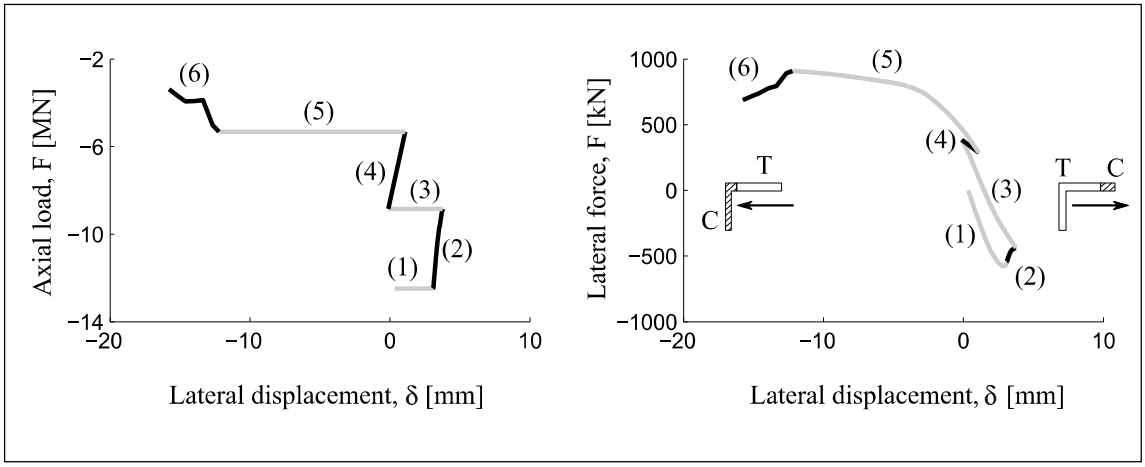

Figure 6-6. Load history with variable axial load for WL.

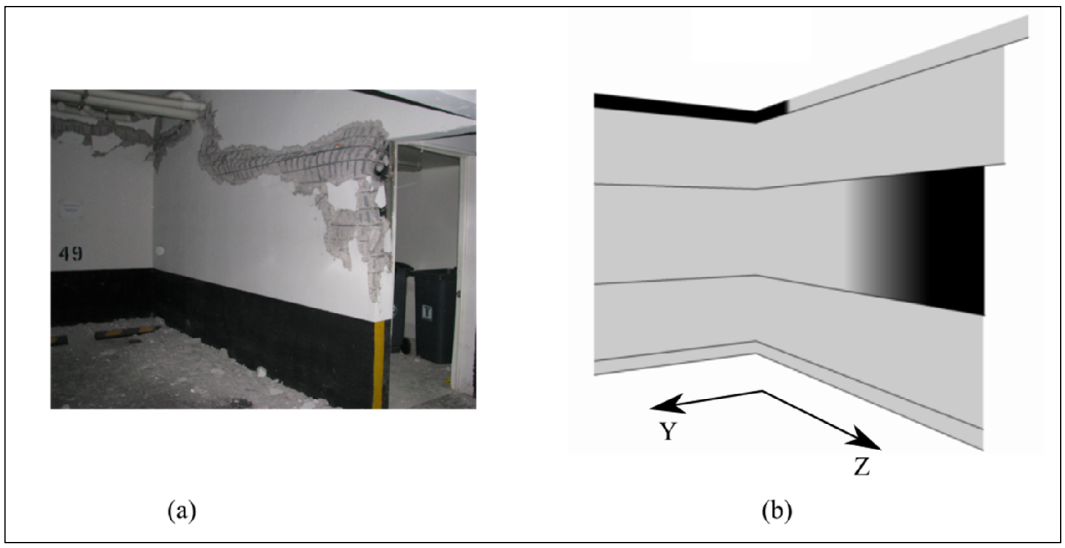

Figure 6-7. Damage reproduction of the reinforced concrete wall WL. a) Actual damage, b) calculated damage (in black).

As shown in Figure 6-7, the inclusion of the right geometry—the irregularity of the wall— allows the model to reproduce the location of damage because if the wall had not had an irregularity, then, it would've failed in the most loaded section—at the end of the element. Figure 6-7(a) shows the actual damage after the 2010, Chile earthquake, while Figure 6-7(b) presents the predicted damage in darker grey or black, according to if the strain in cover concrete of the wall face shown, is more than $\varepsilon_f > 0.004$, twice the amount of the ε_0 used.

7. CONCLUSIONS

This thesis presented a FWE model aimed to capture the cyclic response of slender shear walls similar to those that underwent damage in the 2010, Chile earthquake. These walls were subjected to a wide range of axial loads characterized by ALR=1% to ALR=50%.

In general the analyses showed good agreement between measured and predicted responses and in terms of initial stiffness, peak strength, unloading and reloading stiffness, and ductility. Measured responses were obtained from several walls (rectangular, U-shaped, and T-shaped) tested by different authors under 2D and 3D conditions. It was observed that the pinching phenomenon was accentuated in the predicted response. Based on the good results obtained, the following conclusions can be drawn:

- The FWE element is capable of reproducing the complex cyclic behavior of reinforced concrete shear walls up to a failure condition but shear deformations, bar pull-out, bar fracture in tension, and bar buckling are absolutely necessary to be considered by the model to capture the global cyclic behavior shown by experiments.
- The FWE only requires a-priori calibration of internal parameters when bars fracture in tension, and can give objective responses for a large range of loading conditions with the proposed modification of energy regularization.
- The energy regularization proposed for the bending and shear model enables objective responses in bending and shear, which allows the use of this element for different axial load ratios (ALR) and bending-compression conditions.
- The FWE is numerically efficient even though it includes some shear-coupling effects. Therefore, it is a very attractive choice for 3D inelastic analysis of reinforced concrete shear wall buildings; its application to complete shear wall structures is underway.
- Model assumptions like plane section remaining plane, perfect bond between steel and concrete along the element, and the use of secant unloading-reloading stiffnesses for the shear model, only play a fundamental role in the pinching behavior of the element, which is deemed a small drawback of the proposed model relative to its several other advantages.
- Finally, the FWE can be referred as an improved fiber element since it accounts for shear deformations, can deliver objective results for a high range of axial loads and even for extreme cases where a classic fiber element would fail to converge.

REFERENCES

(INN), I. N. de N. (2010). Diseño estructural - Disposiciones generales y combinaciones de cargas. Santiago, Chile.

ACI Committee 318. (2005). *Building Code Requirements for Structural Concrete* (ACI 318-05.).

Alarcon, C., Hube, M. A., & de la Llera, J. C. (2014). Effect of axial loads in the seismic behavior of reinforced concrete walls with unconfined wall boundaries. *Engineering Structures*, *73*, 13–23. doi:10.1016/j.engstruct.2014.04.047

Arteta, C. A., To, D. V, & Moehle, J. P. (2014). Experimental response of boundary elements of code-compliant reinforced concrete shear walls. In *Tenth U.S. National Conference on Earthquake Engineering*. Anchorage, Alaska. doi:10.4231/D37H1DN29

Belmouden, Y., & Lestuzzi, P. (2007). Analytical model for predicting nonlinear reversed cyclic behaviour of reinforced concrete structural walls. *Engineering Structures*, *29*(7), 1263–1276. doi:10.1016/j.engstruct.2006.08.014

Bertero, V. V. (1980). Seismic behavior of R/C wall structural systems. In *7th world Conference on Earthquake Engineering* (pp. 323–330). Istanbul, Turkey.

Beyer, K., Dazio, A., & Priestley, M. J. N. (2012). Shear Deformations of Slender Reinforced Concrete Walls under Seismic Loading. *ACI Structural Journal*, *2*(108), 167–177.

Brueggen, B. L. (2009). *Performance of T-shaped reinforced concrete structural walls under multi-directional loading*. University of Minnesota.

Ceresa, P., Petrini, L., & Pinho, R. (2007). *Flexure-Shear Fiber Beam-Column Elements for Modeling Frame Structures Under Seismic Loading — State of the Art*. *Journal of Earthquake Engineering* (Vol. 11, pp. 46–88). doi:10.1080/13632460701280237

Coleman, J., & Spacone, E. (2001). Localization issues in nonlinear frame elements. *Modeling of Inelastic Behavior of RC …*, (November), 1257–1265. Retrieved from http://cedb.asce.org/cgi/WWWdisplay.cgi?0101372

Dazio, A., Beyer, K., & Bachmann, H. (2009). Quasi-static cyclic tests and plastic hinge analysis of RC structural walls. *Engineering Structures*, *31*(7), 1556–1571. doi:10.1016/j.engstruct.2009.02.018

Dhakal, R., & Maekawa, K. (2002). Path-dependent cyclic stress–strain relationship of reinforcing bar including buckling. *Engineering Structures*, *24*(11), 1383–1396. doi:10.1016/S0141-0296(02)00080-9

Diana, T. N. O. (2011). Finite Element Analysis User's Manual-Release 9.4. 4. *TNO DIANA*.

Dides, M. a. (2003). *Analisis diámico de estructuras usando elementos con plasticidad concentrada*. Pontificia Universidad Católica de Chile.

Gérin, M., & Adebar, P. (2009). Simple rational model for reinforced concrete subjected to seismic shear. *Journal of Structural Engineering*, *135*(7), 753–762.

Hassan, M., & El-Tawil, S. (2003). Tension Flange Effective Width in Reinforced Concrete Shear Walls. *ACI Structural Journal*, *100*(3), 349–356.

Jansen, D., & Shah, S. (1997). Effect of length on compressive strain softening of concrete. *Journal of Engineering Mechanics*, *2*. Retrieved from http://ascelibrary.org/doi/pdf/10.1061/(ASCE)0733-9399(1997)123:1(25)

Jiang, H., & Kurama, Y. (2010). Analytical modeling of medium-rise reinforced concrete shear walls. *ACI Structural Journal*, (107). Retrieved from http://www.concrete.org/PUBS/JOURNALS/OLJDetails.asp?Home=SJ&ID=51663812

Jünemann, R., Hube, M., Llera, J. D. La, & Kausel, E. (2010). Characteristics of Reinforced Concrete Shear Wall Buildings Damaged During 2010 Chile Earthquake. *Iitk.ac.in*, 2–9. Retrieved from http://www.iitk.ac.in/nicee/wcee/article/WCEE2012_2265.pdf

Karsan, I., & Jirsa, J. (1969). Behavior of concrete under compressive loadings. *Journal of the Structural Division*, *7*(5). Retrieved from http://trid.trb.org/view.aspx?id=105607

Legeron, F., & Paultre, P. (2000). Behavior of high-strength concrete columns under cyclic flexure and constant axial load. *ACI Structural Journal*, (97), 591–601. Retrieved from http://www.concrete.org/Publications/InternationalConcreteAbstractsPortal.aspx?m=details&i=7425

Légeron, F., & Paultre, P. (2003). Uniaxial confinement model for normal-and high-strength concrete columns. *Journal of Structural Engineering*, (February). Retrieved from http://ascelibrary.org/doi/abs/10.1061/(ASCE)0733-9445(2003)129:2(241)

Li, N., Li, Z. X., & Xie, L. L. (2011). A Flexure-Shear Coupling Fiber-Section Model for the Cyclic Behavior of R/C Rectangular Hollow Section Bridge Piers. *Advanced Materials Research*, *374-377*, 2009–2012. doi:10.4028/www.scientific.net/AMR.374-377.2009

MacGregor, J., & Hanson, J. (1969). Proposed Changes in Shear Provisions for Reinforced and Prestressed Concrete Beams*. *ACI Journal Proceedings*, (66), 276–288. Retrieved from http://www.concrete.org/PUBS/JOURNALS/OLJDetails.asp?Home=JP&ID=7360

Maekawa, K., Pimanmas, A., & Okamura, H. (2003). *Nonlinear mechanics of reinforced concrete* (p. 768).

Mander, J., Priestley, M., & Park, R. (1988). Theoretical stress-strain model for confined concrete. *Journal of Structural …*. Retrieved from http://ascelibrary.org/doi/abs/10.1061/(ASCE)0733-9445(1988)114:8(1804)

Massone, L. M., Polanco, P., & Herrera, P. (2014). Experimental and analytical response of RC wall boundary elements. In *Tenth U.S. National Conference on Earthquake Engineering*. doi:10.4231/D39G5GD95

Massone, L. M., & Wallace, J. W. (2004). Load-Deformation Responses of Slender Reinforced Concrete Walls. *Aci Structural Journal*, *101*(101), 103–113. Retrieved from http://www.concrete.org/PUBS/JOURNALS/OLJDetails.asp?Home=SJ&ID=13003

Mazars, J., Kotronis, P., Ragueneau, F., & Casaux, G. (2006). Using multifiber beams to account for shear and torsion. *Computer Methods in Applied Mechanics and Engineering*, *195*(52), 7264–7281. doi:10.1016/j.cma.2005.05.053

McKenna, F., Fenves, G., & Scott, M. (2000). Open system for earthquake engineering simulation. *University of California, Berkeley, CA*. Retrieved from http://scholar.google.com/scholar?hl=en&as_sdt=0,5&cluster=18046361296136611747#0

Mullapudi, R., & Ayoub, A. (2009). Fiber beam element formulation using the Softened Membrane Model. *ACI Special Publication*. Retrieved from http://www.concrete.org/PUBS/JOURNALS/OLJDetails.asp?Home=MJ&ID=51663300

Mullapudi, R. S., Ayoub, A., & Belarbi, A. (2008). A fiber beam element with axial, bending and shear interaction for seismic analysis of RC structures. *Proceedings of the 14th …*. Retrieved from ftp://jetty.ecn.purdue.edu/spujol/Andres/files/05-01-0298.pdf

Nakamura, H., & Higai, T. (2001). Compressive fracture energy and fracture zone length of concrete. *Modeling of Inelastic Behavior of RC …*. Retrieved from http://books.google.com/books?hl=en&lr=&id=NlG-PtPuyJsC&oi=fnd&pg=PA471&dq=Compressive+fracture+energy+and+fracture+zone+length+of+concrete&ots=KYs9XEYDEL&sig=0pKPg6bPLOe9QhreyX8eHGMNVAQ

Pegon, P., Plumier, C., Pinto, A., Molina, J., Gonzalez, P., Colombo, A., … Tirelli, D. (2000). U-shaped walls : Description of the experimental set-up. Ispra, Italy: European Commission, JRC Special Publication No.I.00.141.

Pegon, P., Plumier, C., Pinto, A., Molina, J., Gonzalez, P., Tognoli, P., & Olivier, H. (2000). U-shaped Walls: Quasi-static Test in the Y Direction: Test Report. Ispra, Italy: European Commission, JRC Special Publication No.I.00.143.

Saiidi, M., & Sozen, M. A. (1979). Simple and complex models for nonlinear seismic response of concrete structures. University of Illinois,Urbana (Illinois), USA.

Scott, B., Park, R., & Priestley, M. (1982). Stress-strain behavior of concrete confined by overlapping hoops at low and high strain rates. *ACI Journal Proceedings*, (79), 13–27. Retrieved from http://www.concrete.org/PUBS/JOURNALS/OLJDetails.asp?Home=JP&ID=10875

Scott, M. H., & Fenves, G. L. (2006). Plastic Hinge Integration Methods for Force-Based Beam–Column Elements. *Journal of Structural Engineering*, *132*(2), 244–252. doi:10.1061/(ASCE)0733-9445(2006)132:2(244)

Sherstobitoff, J., Cajiao, P., & Adebar, P. (2012). Analysis and Repair of an Earthquake-Damaged High-rise Building in Santiago, Chile. In *15th world conference on Earthquake Engineering*. Lisboa,Portugal.

Soltani, A., Behnamfar, F., Behfarnia, K., & Berahman, F. (2011). Numerical tools for modeling of RC shear walls. *Proceedings of the 8th …*, (July), 4–6. Retrieved from http://www.eurodyn2011.org/papers/MS02-759.pdf

Song, C., Pujol, S., & Lepage, A. (2012). The Collapse of the Alto Río Building during the 27 February 2010 Maule, Chile, Earthquake. *Earthquake Spectra*, *28*(S1), S301–S334. doi:10.1193/1.4000036

Spacone, E., Filippou, F. C., & Taucer, F. F. (1996). Fibre Beam-Column Model for Non-Linear Analysis of R/C Frames: Part I. Formulation. *Earthquake Engineering & Structural Dynamics*, *25*(7), 711–725. doi:10.1002/(SICI)1096-9845(199607)25:7<711::AID-EQE576>3.0.CO;2-9

Su, R., & Wong, S. (2007). Seismic behaviour of slender reinforced concrete shear walls under high axial load ratio. *Engineering Structures*, *29*(8), 1957–1965. doi:10.1016/j.engstruct.2006.10.020

Suda, K., Murayama, Y., Ichinomiya, T., & Shimbo, H. (1996). Buckling behavior of longitudinal reinforcing bars in concrete column subjected to reverse lateral loading. *Proc., 11th World Conf. on …*. Retrieved from http://scholar.google.com/scholar?hl=en&btnG=Search&q=intitle:Buckling+behavior+of+longitudinal+reinforcing+bars+in+conrete+column+subjected+to+reverse+lateral+loading#0

Vecchio, F. J., & Collins, M. P. (1986). The modified compression field theory for reinforced concrete elements subjected to shear. *ACI Journal*, *83*(22), 219–231.

Wood, S., Wight, J., & Moehle, J. (1987). The 1985 Chile earthquake: observations on earthquake-resistant construction in Viña del Mar, (February 1987). Retrieved from http://www.ideals.illinois.edu/handle/2142/14145

Zhang, Y., & Wang, Z. (2000). Seismic behavior of reinforced concrete shear walls subjected to high axial loading. *ACI Structural Journal*, (97), 739–750. Retrieved from http://www.concrete.org/Publications/ACIMaterialsJournal/ACIJournalSearch.aspx?m=details&ID=8809

Zhao, J., & Sritharan, S. (2007). Modeling of strain penetration effects in fiber-based analysis of reinforced concrete structures. *ACI Structural Journal*, (104), 133–141. Retrieved from https://pantherfile.uwm.edu/jzhao/www/Bond_SP01_pages/ACI Bond Paper_JZ_SS.pdf

APPENDICES

Appendix A: Mechanical parameters for WSH2

Figure A-1 shows a graphical user interface (GUI) developed for this thesis, where a triangular mesh used for the rectangular wall WSH2 is displayed. For clarity, only the left part of the walls is shown. The triangular mesh was achieved by using the PDE toolbox from MATLAB. Triangles were chosen because it's the simplest polygon capable of fitting into any other polygon. Cover, unconfined and confined concrete fibers are indicated in yellow, light blue and green (steel bars are shown in red) and the number of fibers used for this wall were 1349, 2772 and 464 respectively

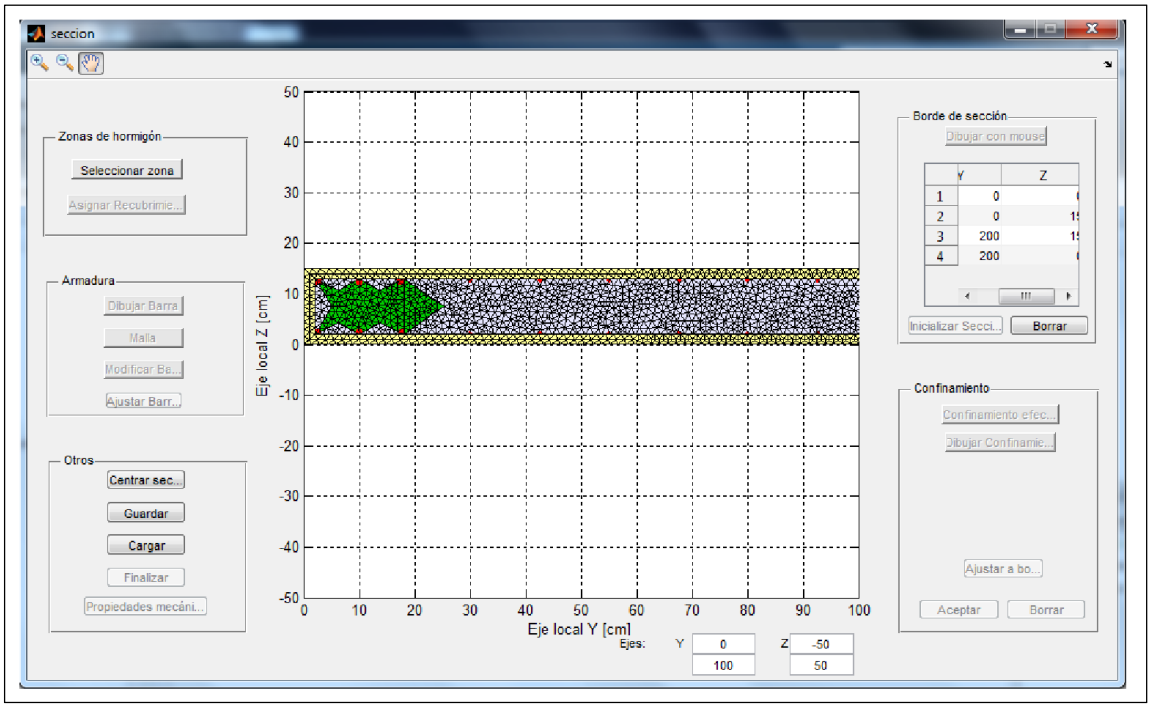

Figure A-1. GUI showing the mesh of the wall WSH2

In this case, the peak concrete strength is $f_c' = 40.5\ MPA$, the yield stress of stirrups is $f_{yh} = 485\ MPA$ and the spacing between stirrups is $75\ mm$.

The unconfined concrete energy was calculated by using the formula proposed by (Nakamura & Higai, 2001), $G_{un} = 8.8 \cdot \sqrt{f_c'} = 56\ MPAmm = 0.056\ MPAm$. The cover concrete energy was computed from a typical $\sigma - \varepsilon$ curve, so that the deformation at peak strength is $\varepsilon_0 = 0.002$ and the deformation where $\sigma = 0.2 f_c'$ is $\varepsilon_r = 0.007$ for a 30 cm tall cylinder. Therefore, the cover concrete energy was $0.041\ MPa - m$.

Finally, for the confined concrete peak strength and the corresponding deformation, the Kent & Park model was used, while for the fracture energy, the average between results from (B. Scott et al., 1982) and (Légeron & Paultre, 2003) was selected. This is because fracture energy plays an important role in ductility of elements.

For the Kent&Park model the volumetric ratio of transverse reinforcement is $\rho_s = \frac{V_s}{V_c} = 0.0119$, where V_s is the total volume of stirrups and V_c is the volume of core concrete which was calculated from center to center of stirrups in all directions. Following the typical formulas, the new peak strength and its corresponding deformation are $f_{cc} = 46.25\ MPA$ and $\varepsilon_{cc} = 0.0023$ respectively. Then the area under the confined $\sigma - \varepsilon$ curve up to ε_r is $0.59\ MPA$ and then the fracture energy is $G_{cc} = 0.23\ MPAm$.

Once the fracture energy is computed, it is necessary to transform that energy into effective parameters as explained in the section 4. The total area of unconfined concrete inside the core is $A_{un} = \frac{8^2}{8} \cdot 4 + \frac{10.2^2}{8} = 45\ cm^2$. Please note that there are only 5 light blue triangles inside the core as seen in Figure A-1 because on side is confined due to the concrete of the wall in that direction. The total core area is $A_{tot} = 184.7\ cm^2$ then the effective confined area inside the core is $A_c = 139.7\ cm^2$. Hence:

$$G_{cc}^{eff} = \frac{G_{cc} \cdot A_c + G_c \cdot A_{un}}{A_c} = 0.292\ MPa - m \tag{7}$$

The green area outside the core was assigned the same energy. For other properties such as f_{cc} and ε_{cc} it was followed the same procedure.

Now, the energy from Légeron & Paultre is a bit more cumbersome, but some key parameters are the reference length which was assume to be the one from unconfined concrete (Nakamura & Higai, 2001) : $L_c = \frac{1300}{\sqrt{f_c'}} \cdot \frac{1}{981} = 20.43\ cm$, the geometrical effectiveness coefficient $K_e = \frac{A_c^{eff}}{A_{tot}} = \frac{126.66}{17\ 6} = 0.72$ and the transverse volumetric ratio $\rho_s = 0.0142$. Please note that some values are different depending on how the properties were measured. Moreover, A_c^{eff} is different from A_c since the latter is the one using triangles instead of parabolas. With all this data, the deformation where $\sigma = 0.5 f_c'$ is $\varepsilon_{50} = 0.0404$. With the length associated the confined energy is $0.28 MPa - m$. However this is for the whole core, then, using Equation 7 this value increases up to $0.35\ MPa - m$. Finally the average value for fracture energy is $G_{cc} = 0.323\ MPa - m$.